Transition Prediction in Hypersonic Boundary Layers Using Receptivity and Freestream Spectra

P. Balakumar* and Amanda Chou†
Flow Physics and Control Branch
NASA Langley Research Center, Hampton, VA 23681

Boundary-layer transition in hypersonic flows over a straight cone can be predicted using measured freestream spectra, receptivity, and threshold values for the wall pressure fluctuations at the transition onset points. Simulations are performed for hypersonic boundary-layer flows over a 7-degree half-angle straight cone with varying bluntness at a freestream Mach number of 10. The steady and the unsteady flow fields are obtained by solving the two-dimensional Navier-Stokes equations in axisymmetric coordinates using a 5th-order accurate weighted essentially nonoscillatory (WENO) scheme for space discretization and using a third-order total-variation-diminishing (TVD) Runge-Kutta scheme for time integration. The calculated N-factors at the transition onset location increase gradually with increasing unit Reynolds numbers for flow over a sharp cone and remain almost the same for flow over a blunt cone. The receptivity coefficient increases slightly with increasing unit Reynolds numbers. They are on the order of 4 for a sharp cone and are on the order of 1 for a blunt cone. The location of transition onset predicted from the simulation including the freestream spectrum, receptivity, and the linear and the weakly nonlinear evolutions yields a solution close to the measured onset location for the sharp cone. The simulations overpredict transition onset by about twenty percent for the blunt cone.

Nomenclature

C_{recpt} = receptivity coefficient

c_v = specific heat

E = total energy

* Research Scientist, Associate Fellow AIAA
† Research Scientist, Member AIAA

e = internal energy

F = flux vector in the x-direction

f = frequency in Hz

G = flux vector in the r-direction

k = thermal conductivity

M = Mach number

N = N factor

Pr = Prandtl number

P_s = Mean surface pressure, Pa

p = pressure, Pa

PSD = power spectral density

$\boldsymbol{Q}$ = conserved flow variables vector

R = gas constant, J/(kg*K)

R_n = nose radius, mm

Re = unit Reynolds number, per meter

Re_s = Reynolds number based on the distance s

r = radial coordinate

rms = root mean square

S = source term or entropy

s = distance along the surface, m

T = temperature, K

t = time

U = mean axial velocity

u = axial velocity

V = radial velocity

X = axial coordinate, cm

x_0 = reference x location

Y = radial coordinate or the normal to the surface, cm

α = wavenumber in the x-direction

η = curvilinear coordinate in the radial direction, boundary-layer similarity coordinate

δ = boundary layer thickness

γ = specific heat ratio

μ = viscosity

ξ = curvilinear coordinate in the axial direction

ρ = density

ω = frequency in radians

Subscripts

ac = acoustic

e = boundary-layer edge conditions

max = maximum

n = normal to the surface, neutral point

o = stagnation condition

s = surface

T = transition location

w = wall

∞ = freestream quantities

I. Introduction

Accurate prediction of transition onset and transition end points, as well as modeling of the transitional and turbulent regions, are major concerns when using CFD codes to compute aerodynamic quantities such as lift, drag, skin friction, and heat transfer. Transition from a laminar to a turbulent state in shear flows occurs due to the evolution and interaction of different disturbances inside the shear layer. Although there are several mechanisms and routes to go from a laminar to a turbulent state, most of the routes in quiet environments generally follow these fundamental processes:[1]

1. Receptivity
2. Linear instability

3. Nonlinear stability and saturation

4. Secondary instability and breakdown to turbulence

In the receptivity process, unsteady disturbances in the environment interact with the boundary layer and/or with the inhomogeneities in the geometry to generate instability waves inside the shear layer. In quiet environments, the initial amplitudes of these instability waves are small compared to any characteristic velocity, density, and temperature scales in the flow. In the second stage, the amplitudes of these instability waves grow exponentially downstream and this process is described by the linearized Navier-Stokes equations. Further downstream, the amplitudes of the disturbances become large and the nonlinear effects inhibit the exponential growth and the amplitude of the waves eventually saturate. In the next stage, the finite-amplitude saturated disturbances become unstable to two- and/or three-dimensional disturbances. In this stage, the secondary instability appears and the spectrum broadens due to complex interactions and further instabilities. The flow becomes turbulent within a short distance downstream. When the disturbances reach large amplitudes due to exponential growth, the nonlinear effects set in and the mean flow becomes distorted. As a result of this distortion, local skin friction and heat transfer rates increase from their respective laminar values. The location where they start to deviate from the laminar values is defined as the transition onset point. Hence transition onset is determined by three factors: (1) the initial amplitudes of the instability waves, (2) the growth rates of the instability waves, and (3) the threshold value for the amplitude of the instability waves at which transition onset will occur.

Most of the research in hypersonic boundary layer transition is concerned with the characteristics of the instability waves, especially the growth rates and the evolution of the second mode in flows over flat plates and cones.[2-12] Linear stability computations and PSE (Parabolized Stability Equations) computations have been performed and compared with experiments.[13-14] The transition prediction methods such as the N-factor method[15-17] are based on the growth rates for a single frequency. This method works reasonably well when the N-factors at transition onset are correlated very well with a particular tunnel. Even a well-calibrated fixed N-factor for a particular tunnel is not sufficient for transition prediction, because the N-factor at transition onset depends on the unit Reynolds number. The unit Reynolds number effect is explained by the fact that the most-amplified second mode frequencies increase with unit Reynolds number and the noise level decreases with increasing frequency. The second factor is that the nose Reynolds number increases with the unit Reynolds number and the transition heavily depends on the nose Reynolds number.[18, 19]

Hence, to remove the uncertainties associated with using the N-factor to predict transition onset, the effects of the freestream disturbances in the transition process must be included. The receptivity process in hypersonic flows has been investigated for flow over flat plates, wedges, and cones at different flow conditions.[20] It was found that amplitudes of the instability waves generated by the slow acoustic freestream disturbances are about 3-5 times the amplitude of the freestream disturbances. The next part of the problem is to determine criteria that can be used to estimate the transition onset point. Here, the experimental and direct numerical simulations results provide some threshold values for the amplitude of the disturbances near the transition onset location. The experiments[21] show that the transition onset occurs when the root mean square (rms) of the pressure fluctuations at the wall normalized by the mean boundary layer edge reaches a value between 0.1 and 0.2. The rms values are generally obtained from a finite band of frequencies. In the N-factor methods, a single frequency is considered in the estimation of transition onset location. To follow the single frequency approach, all of the energy in the spectrum would be assigned to the most-amplified frequency. This is not physically correct because, in reality, the disturbance growth rates strongly depend on the frequency. Hence, assigning all the energy into one frequency overestimates the amplitude levels in the boundary layer.

Another issue that arises in these transition prediction methods is that when the normalized rms values of the pressure fluctuations reach 0.1 and 0.2, nonlinear effects will set in. As the process is no longer linear, weakly nonlinear effects must be included in the prediction method. One approach is to divide the frequency spectrum into small bins and to replace the energy in these bins by the amplitude of energy assigned to the single middle frequency. Mack[22] proposed this idea in his amplitude-based transition prediction method. Later, Fedorov[23] also used this method to predict transition in hypersonic boundary layers. This is the approach adapted for the work presented in this paper. The first step is to divide the measured freestream spectra into small bins and to compute the amplitude of the central frequency. The second step is to superimpose all the frequencies with these computed amplitudes at the outer boundary of the domain and to perform simulations to determine the evolution of the disturbances inside the boundary layer. The final step is to determine the transition onset location using a threshold value for the disturbances. This method considers the freestream spectrum, the receptivity process, linear and weakly nonlinear evolution of the disturbances, and a threshold value for the amplitudes of the disturbances to estimate the transition onset location. The objective of this paper is to predict the transition location on a 7° half-angle cone at a freestream Mach number of 10 at different unit Reynolds numbers using this approach. The

predicted transition and stability will be compared with the experiments performed at the Arnold Engineering Development Center (AEDC) Hypervelocity Wind Tunnel 9.[21, 24] Stability and N-factor computations were also performed[21, 24, 25] using the STABL code[17] for different cases and good agreement between the computed and measured amplification rates and most-amplified frequencies were observed for sharp and moderately blunted cones.

In Sec. 2, the model parameters and the flow conditions simulated in this paper are given. In Sec. 3, the governing equations and the solution algorithms used in the simulations are briefly described. The form and the estimation of the amplitudes of the acoustic field imposed in the outer boundary are also described in this section. In Sec. 4, the computational results are presented. The results include mean flow profiles, N-factors obtained from linear stability and PSE computations, receptivity coefficients for single waves, and the transition onset points obtained from the simulations with multiple frequencies. In Sec. 5, the conclusions drawn from this investigation are given.

II. Models and Flow Conditions

A large amount of boundary-layer transition and stability data were obtained at Mach 10 in the Arnold Engineering Development Center (AEDC) Hypervelocity Wind Tunnel 9 on a 1.5-m-long 7° half-angle cone at unit Reynolds numbers between 1.8 and 31 million per meter.[24] The nose radius of the cone was varied from 0.152 to 50.8 mm. The transition onset locations were determined using coaxial thermocouples and temperature sensitive paint. The stability measurements were obtained using high-frequency response pressure sensors. This paper presents the simulation results for two nose radii, R_n = 0.152 and 5.08 mm.

Computations were performed for the five cases given in Table 1. We also included the corresponding experimental run number provided in Ref. 24 in the first column of the Table 1. The freestream conditions were selected to match the experimental conditions. The freestream Mach numbers and the unit Reynolds numbers for the sharp nose R_n = 0.152 mm case are (9.39, $2.03*10^6$/m), (9.60, $7.03*10^6$/m), and (9.86, $16.25*10^6$/m). The corresponding Reynolds numbers based on the nose radius are 308, 1068, and 2470, respectively. We referred these three cases as Case 1, 2, and 3, respectively. Similarly, the freestream Mach numbers and the unit Reynolds numbers for the medium blunt nose R_n = 5.08 mm case are (9.81, $18.17*10^6$/m), and (10.0, $31.8*10^6$/m). The corresponding Reynolds numbers based on the nose radius are 92304, and 157886, respectively. We referred these two cases as Case 4, and 5, respectively. The wall temperature is fixed at 0.30 times the freestream stagnation temperature. The

Prandtl number, specific gas ratio, and the gas constant are Pr = 0.74, γ = 1.4, and R = 297 J/(kg*K), respectively. The Sutherland viscosity law of the following form is used to compute the viscosity:

$$\mu = 1.458 * 10^{-6} \frac{T^{1.5}}{(T + 102.7K)}. \quad (1)$$

Marineau et al. [24, 21] used slightly different equations based on a curve fit to the experimental data to calculate the viscosity in computing the unit Reynolds numbers. This caused about 10% differences between the unit Reynolds numbers given in Table 1 and in Ref. 24.

Table 1: Test Conditions

Case	R_n (mm)	P_o (MPa)	T_o (K)	M_∞	p_∞ (kPa)	T_∞ (K)	Re (1E6/m)
1 (3745)	0.152	2.3	982	9.39	82.34	52.69	2.03
2 (3743)	0.152	8.9	1018	9.60	275.15	52.38	7.03
3 (3742)	0.152	22.6	1035	9.86	584.97	50.62	16.25
4 (3746)	5.08	22.7	978	9.81	607.78	48.30	18.17
5 (3748)	5.08	43.4	1016	10.00	1022.64	48.38	31.08

III. Governing Equations

The governing equations are the two-dimensional unsteady compressible Navier-Stokes equations, written in conservation form and in cylindrical coordinates:

$$\frac{\partial}{\partial t} rQ + \frac{\partial rF}{\partial x} + \frac{\partial rG}{\partial r} = S, \quad (2)$$

$$Q = \begin{bmatrix} \rho \\ \rho E \\ \rho u \\ \rho v \end{bmatrix}. \tag{3}$$

Here, *(x, r)* are the cylindrical coordinates, (*u, v*) are the velocity components, ρ is the density, and p is the pressure. The total energy, E, is given by:

$$E = e + \frac{u^2 + v^2}{2},$$

$$e = c_v T, \; p = \rho RT, \tag{4}$$

where e is the internal energy and T is the temperature. The fluxes *F, G,* and the source term *S* are described in Kara *et al*.[19] The viscosity, μ, is computed using Sutherland's law Eq.(1). The second coefficient of viscosity is assumed to be $-2/3\mu$ and the thermal conductivity, k, is given in terms of the Prandtl number, Pr. The variables ρ, p, T and velocity are nondimensionalized by their corresponding reference variables ρ_∞, p_∞, T_∞ and $\sqrt{RT_\infty}$ respectively. The reference value for length is given by $\sqrt{\nu x_0 / U_\infty}$, where x_0 is a reference location. For the computations, the equations were transformed from the physical coordinate system (*x, r*) to the computational curvilinear coordinate system (ξ, η) in a conservative manner.

Solution Algorithm

The governing equations are solved using a 5th-order accurate weighted essentially nonoscillatory (WENO) scheme for space discretization and using a third order total-variation-diminishing (TVD) Runge-Kutta scheme for time integration. Shu[26] explains the WENO and TVD methods. Atkins[27] gives the application of the essentially non-oscillatory (ENO) method to the N-S equations. Balakumar[28] and Kara et al.[29] describe in detail the solution method implemented in this computation.

At the outflow boundary, an extrapolation boundary condition is used. At the wall, we use viscous conditions for the velocities and compute density from the continuity equation. In the mean flow computations, we prescribe the freestream values at the outer boundary, which lies outside the bow shock. The angle of attack is zero in all of the cases computed here. In the unsteady computations, the acoustic perturbations are superimposed on the uniform mean flow at the upper boundary. The procedure is to compute the steady mean flow first by performing unsteady

computations using a variable time step until the maximum residual reaches a small value ~10^{-11}. The next step is to introduce unsteady disturbances at the upper boundary of the computational domain and to perform time-accurate computations to investigate the interaction and evolution of these disturbances downstream. The grid is generated using analytical formulae. The grid stretches in the η direction close to the wall and is uniform outside of the boundary layer. In the ξ direction, the grid is symmetric about the leading edge and very fine near the nose and is uniform in the flat region.

The measured freestream broadband acoustic field[21] (Fig. 1) that impinges on the outer boundary is modeled by an equivalent series of discrete Fourier acoustic modes as shown in Fig. 2(a).

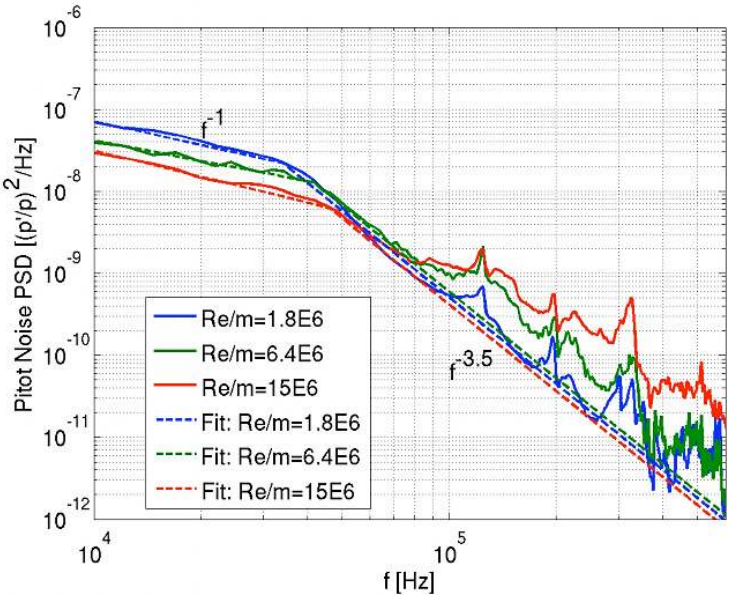

Figure 1. Freestream pressure fluctuations in the AEDC Tunnel 9, by Marineau et al.[21]

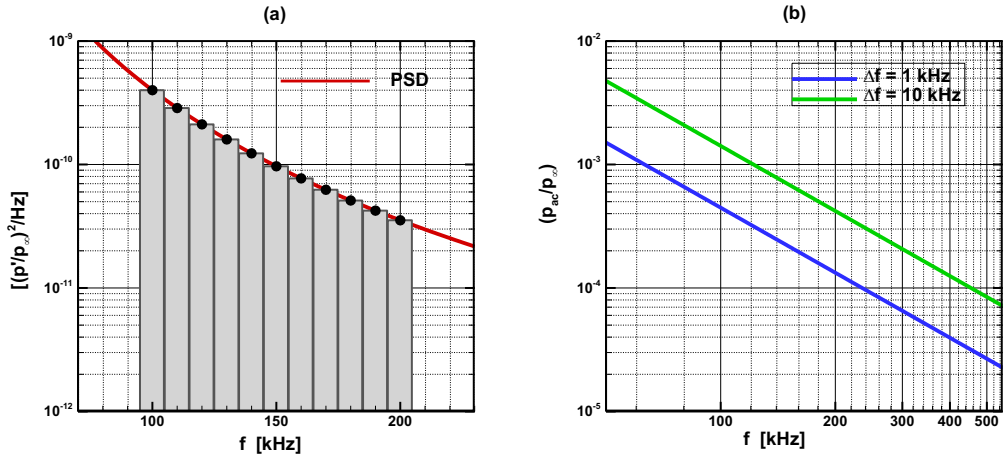

Figure 2. Computations of the amplitudes of the freestream acoustic disturbances. (a) PSD and the bins used to compute the energy, and (b) computed amplitudes based on bin sizes of 1 and 10 *kHz*.

The discrete acoustic field is taken to be in the following form,

$$p_{ac}(x,t) = \sum_{nf=1}^{nf\,max} \left(\tilde{p}_{ac,nf} e^{i(\alpha_{ac,nf} x - \omega_{nf} t + \phi_{nf})} + c.c. \right) \quad . \tag{5}$$

$$\omega_{nf} = 2\pi f_{nf},$$
$$f_{nf} = f_{min} + (nf - 1)\Delta f.$$

Here *nfmax* is the number of discrete modes considered in the simulation, $\alpha_{ac,nf}$ is the x wavenumber of the acoustic wave, ω_{nf} is the corresponding frequency in radians of the acoustic disturbance, f_{nf} is the frequency in *Hz*, f_{min} is the lower bound of the frequencies considered, Δf is the width of each bin, and c.c. refers to the complex conjugate of the first term. The frequency parameters are selected to cover all the unstable frequencies centered around the most amplified frequency.

The amplitude $\tilde{p}_{ac,nf}$ is evaluated from the measured PSD of the freestream pressure fluctuations shown in Fig.1. The power spectral density for a disturbance given by Eq. (5) is

$$\left(p_{ac,nf} \right)_{PSD} = 2\left(\tilde{p}_{ac,nf} \right)^2 \tag{6}$$

The measured spectrum at high frequencies can be approximated by

$$\left(p_{ac,nf}\right)_{PSD} = C\, f_{nf}^{-3.5} \,/\, Hz \tag{7}$$

where f_{nf} is the frequency in *Hz* and C is a constant determined from the measurement (Fig.1). The estimated value of C in this case is $C = 126.5*10^6$. Equating Eqs. 6 and 7 we determine the amplitude $\tilde{p}_{ac,nf}$ from

$$2\left(\tilde{p}_{ac,nf}\right)^2 = C\, f_{nf}^{-3.5} \Delta f. \tag{8}$$

Figure 2(b) depicts the magnitude of $\tilde{p}_{ac,nf}$ for two bin sizes of Δf =1 and 10 *kHz*. The approximate amplitudes at 100, 200, 300, 400 and 500 *kHz* using the bin size of 1 *kHz* are $4.5*10^{-4}$, $1.3*10^{-4}$, $6.5*10^{-5}$, $3.9*10^{-5}$, and $2.7*10^{-5}$, respectively. It is seen that the amplitude of the acoustic wave with a frequency of 500 *kHz* is about 16 times smaller than that for the 100 *kHz* acoustic wave. This amplitude ratio is equivalent to an N-factor of 2.7.

IV. Results

(a) Mean Flow

Figures 3(a) and 3(b) show the mean flow density contours computed using the WENO code for Case 3. Figure 3(a) depicts the flow field for the entire domain and Fig. 3(b) shows the results for the nose region. Figures 4, 5, and 6 depict the boundary-layer density profiles at different axial locations in physical and similarity coordinates for Cases 1, 2, and 3, respectively. The boundary-layer profiles slowly approach the similarity profile close to x = 4.0 cm for Cases 1 and 2 and close to x = 10 cm for Case 3.

Similarly, Figures 7, 8 and 9 show the mean flow results for the blunt nose Cases 4 and 5. The experiments and computations[18, 19] have shown that nose bluntness stabilizes hypersonic boundary layers. This is due to the formation of a strong entropy layer across the bow shock. This entropy layer persists for a long distance before it merges with the developing boundary layer along the wall. Figures 7(a) and (b) depict the entropy contours for the sharp and blunt nose Cases 3 and 4, respectively. For the sharp nose case, a small entropy layer appears near the nose and it merges with the boundary layer within a short distance from the nose. For the larger nose radius case, the entropy layer that is visible near the nose region, persists downstream for a long distance and eventually merges with the boundary layer. Figures 8(a) and (b) show the density and entropy profiles at different axial locations for the Case 4. Up to x = 50 cm, no discernable boundary layer for the blunt nose case exists near the wall. The boundary layer

thickness at x = 20 cm for Case 3 (Fig. 6(a)), is about 0.075 cm. In contrast, it is about 1.0 cm for the blunt nose case. Figure 8(b) clearly shows the entropy layer in the outer part of the boundary layer. The outside entropy layer merges with the boundary layer near the wall close to x = 50.0 cm. The entropy layer and the boundary layer in non-dimensional units merge approximately 100 nose radii downstream from the nose. Similarly, Figs. 9(a) and (b) show the density and the entropy profiles at different axial locations for Case 5. There are no noticeable quantitative differences between the profiles for Cases 4 and 5.

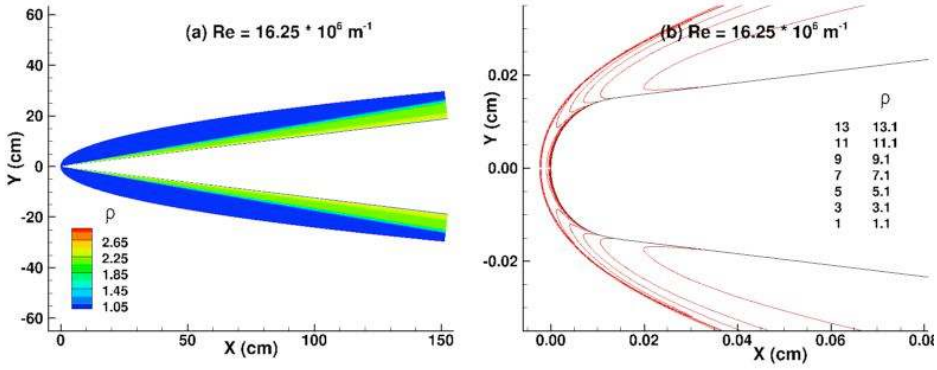

Figure 3. Computed mean density contours for Case 3. (a) Entire domain, and (b) near the nose region.

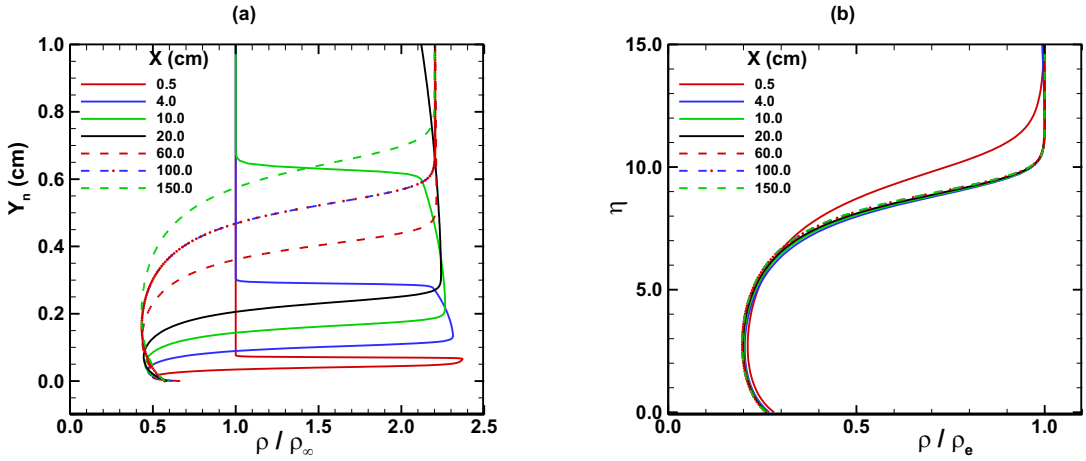

Figure 4. Boundary layer density profiles (a) in physical and (b) similarity coordinates at different axial locations for Case 1.

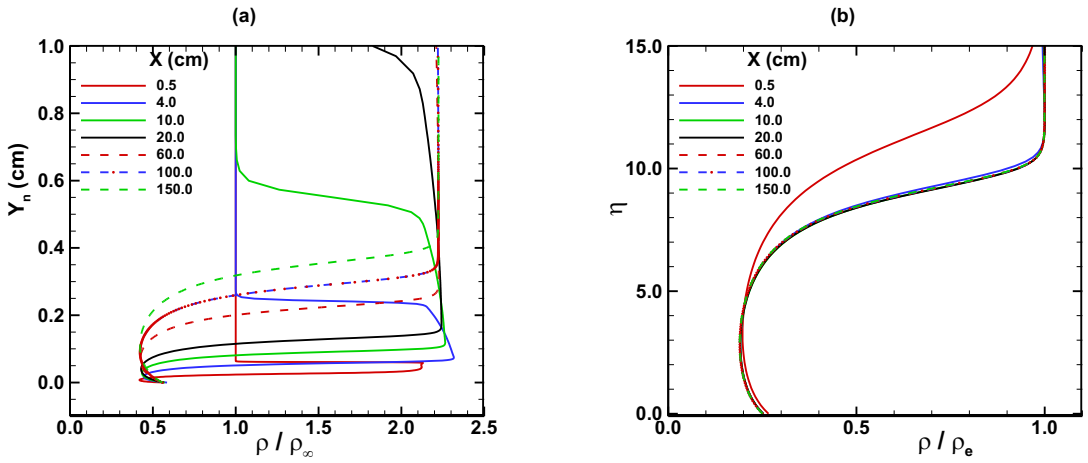

Figure 5. Boundary layer density profiles (a) in physical and (b) similarity coordinates at different axial locations for Case 2.

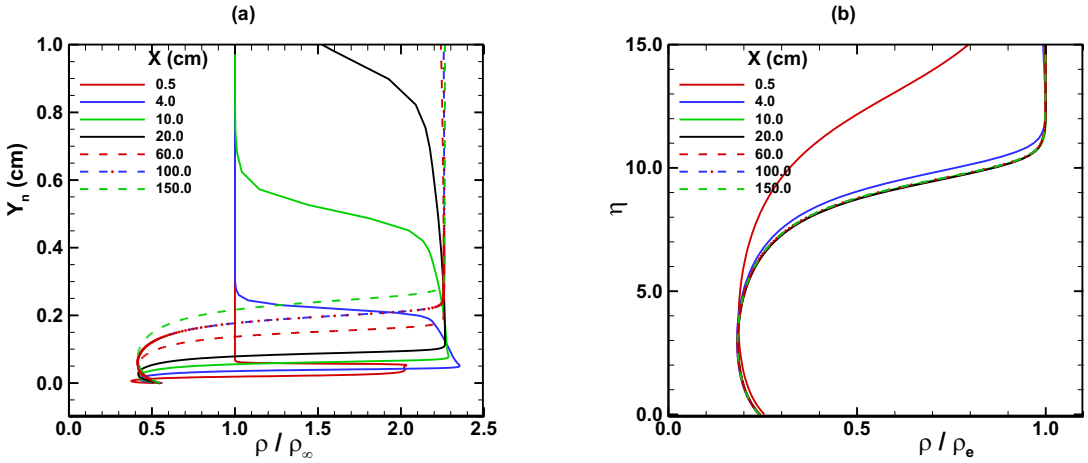

Figure 6. Boundary layer density profiles (a) in physical and (b) similarity coordinates at different axial locations for Case 3.

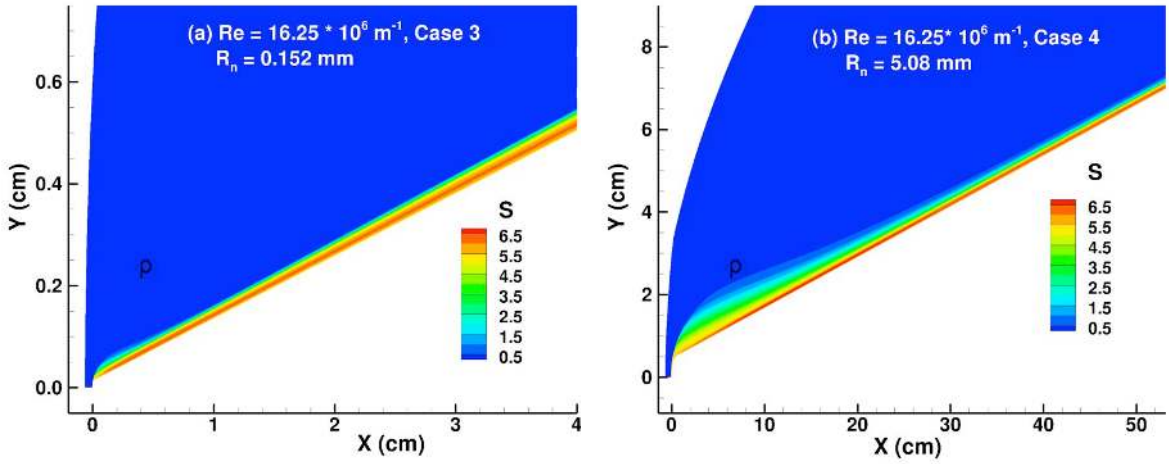

Figure 7. Contours of entropy for flow over the (a) sharp (Case 3), and (b) blunt (Case 4) cones (not to scale).

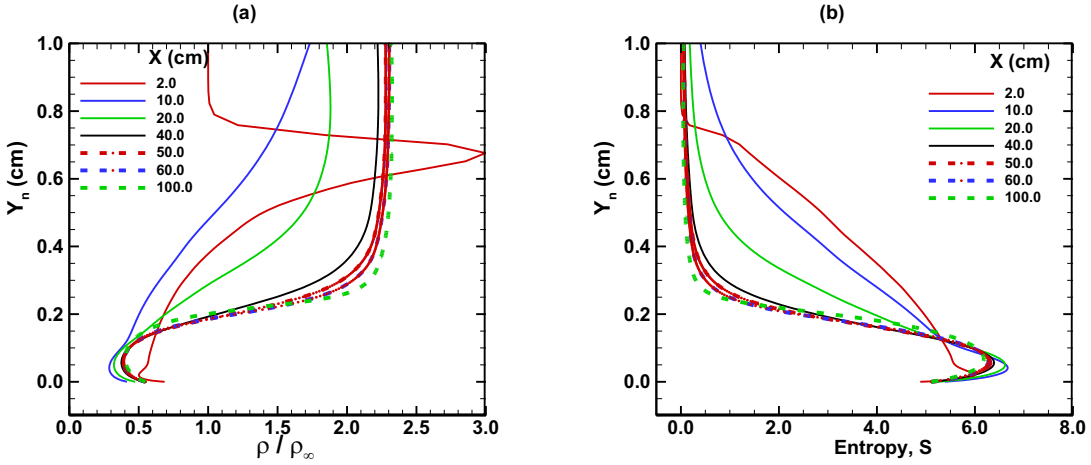

Figure 8. Boundary layer profiles at different axial locations for Case 4. (a) density, (b) entropy.

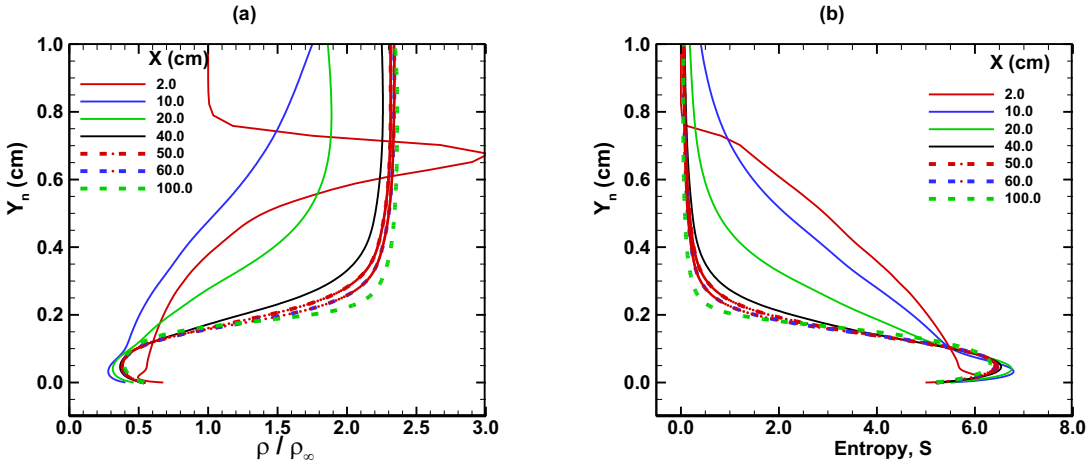

Figure 9. Boundary layer profiles at different axial locations for Case 5. (a) density, (b) entropy.

(b) Linear Stability

Linear stability analysis and parabolized stability equations (PSE) analysis were performed on the computed boundary layer profiles for the Cases 1-5. Figures 10(a-e) show the computed N-factors using parallel linear stability and PSE for Cases 1-5, respectively. The measured transition onset locations are also marked in each of the figures and are given in Table 2. The measured transition onset locations for the Cases 1-5 are x_{Tcase1} = 84 cm, x_{Tcase2} = 36 cm, x_{Tcase3} = 25 cm, x_{Tcase4} = 68 cm, and x_{Tcase5} = 68 cm, respectively. The maximum N-factors at the transition onset locations obtained from the PSE computations based on $(\rho u)_{max}$ are N_{case1} = 4.0, N_{case2} = 5.1, N_{case3} = 6.7, N_{case4} = 3.0, and N_{case3} = 3.0. The corresponding peak frequencies at transition onset for Cases 1, 2, 3, 4, and 5, are 90, 260, 460, 210 and 270 kHz, respectively. It is seen for sharp nose cases that the N-factors at the transition onset location increase with unit Reynolds numbers. The frequencies increased by approximately 3 and 5 times for Cases 2 and 3, respectively, when compared to Case 1. The unit Reynolds number increased from $2.03*10^6$/m for Case 1 to $7.03*10^6$/m and $16.25*10^6$/m for Cases 2 and 3, respectively.

Table 2: Computed and measured transition onset points.

Case	R_n(mm)	Re (1E6/m)	X_T (cm)			N-Factor (PSE)	Freq. (kHz)
			$(p_{rms})_T / P_s$		Expt.		
			0.1	0.2			
1	0.152	2.03	60	76	84	4.0	90
2	0.152	7.03	28	36	36	5.1	260
3	0.152	16.25	17	21	25	6.7	460
4	5.08	18.17	92	96	68	3.0	210
5	5.08	31.08	90	93	68	3.0	270

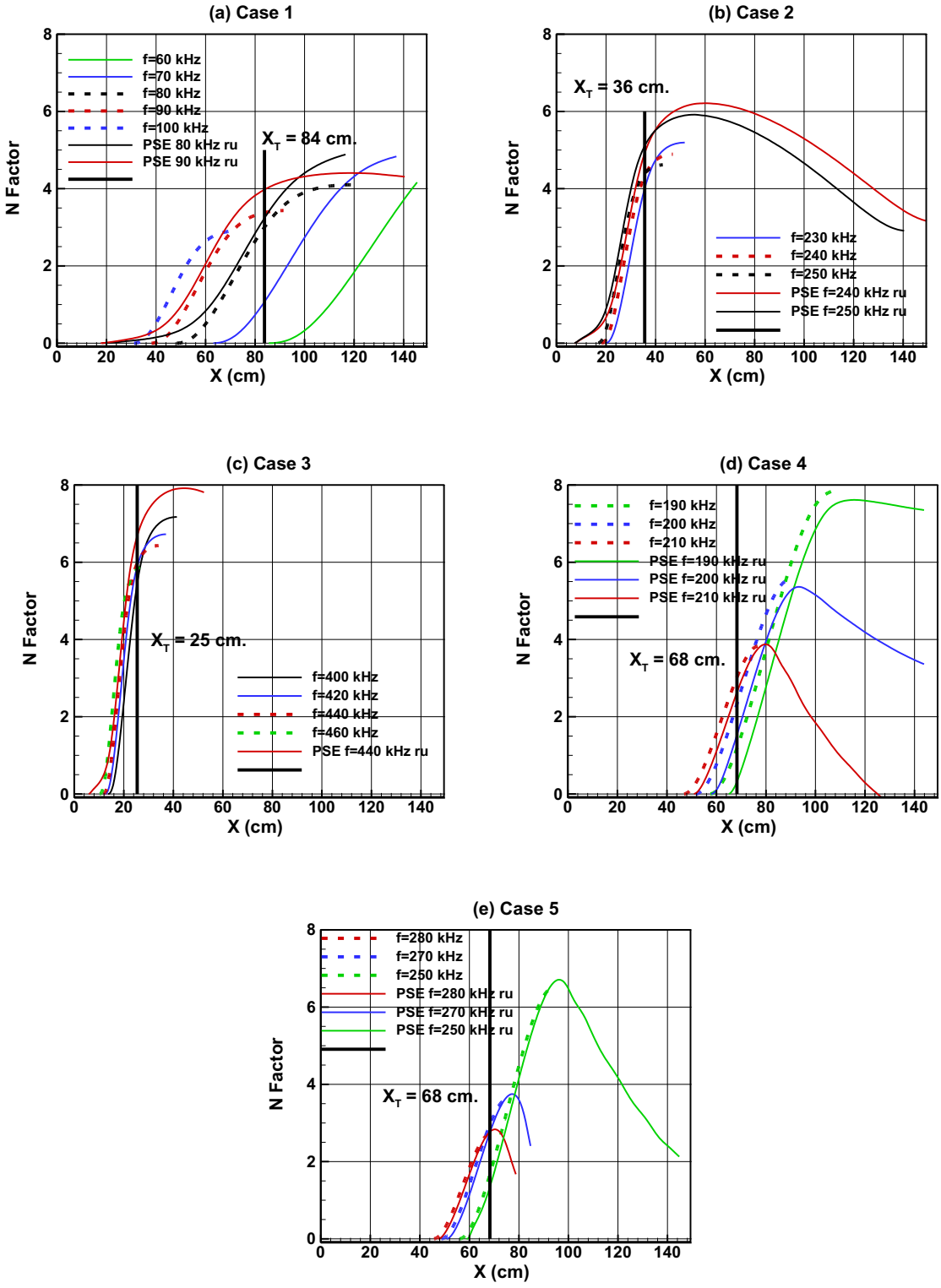

Figure 10. N-factor curves computed from the linear stability analysis and the PSE analysis based on $(\rho u)_{max}$ for the (a) Case 1, (b) Case 2, (c) Case 3 , (d) Case 4, and (e) Case 5.

To estimate the expected dominant frequency bands near transition onset, the variation of the N-factors near the transition onset points with respect to frequency are plotted in Figs. 11 and 12. In these figures, receptivity analysis and the freestream amplitude variations are not considered in the analysis. Figure 11 displays the results for the sharp cone Cases 1, 2, and 3 at the stations x = 83, 35 and 25 cm, respectively, and Fig. 12 shows the results for the blunt cone Cases 4 and 5 at stations x = 70 and 80 cm, respectively. We also included the maximum N-factors and the corresponding frequencies for each case in the figures.

The first observation is that the width of the unstable frequency band increases significantly with the unit Reynolds number for the sharp cone cases. To obtain an estimate for the bandwidth of the expected frequencies, a horizontal line at two less than the maximum N-factor values was drawn. The difference of two in N-factor corresponds to an amplitude reduction of approximately 8 times from the amplitude at the maximum N-factor. The estimated bandwidths for the Cases 1, 2 and 3 are (70-130), (210-370), and (380-690) *kHz*, respectively. The results for the blunt nose, Cases 4 and 5, show that the unstable frequency bands are very narrow compared to the sharp cone case. It is to be also noted that the measured transition onset location for Cases 4 and 5 occurred at almost the same location: x = 68 cm. In the experiment, there was an uncertainty in detecting the onset location of about 13 cm in the measurements corresponding to Cases 4 and 5. Hence, the estimated transition location is approximately between 68 and 81 cm. The estimated bandwidths at x = 70 and 80 cm are (190-230) and (180-215) kHz for Case 4 and they are (240-290) and (240-275) for Case 5. It is seen that the unstable frequency bandwidths are very narrow, about 40-50 kHz, for flows over blunt cones compared to 300 kHz for the sharp cone cases at comparable Reynolds numbers.

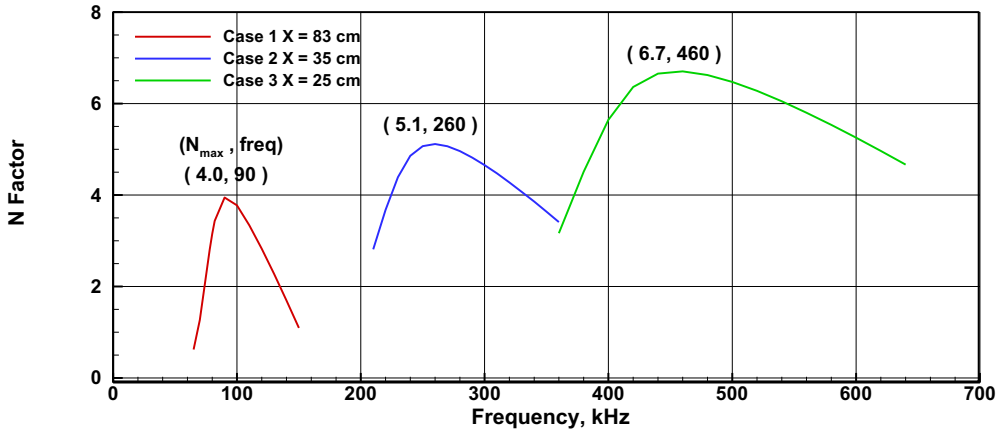

Figure 11. Variation of N-factors with respect to frequency at locations near the measured transition onset points, computed from the PSE analysis and based on $(\rho u)_{max}$ for the Cases 1, 2, and 3.

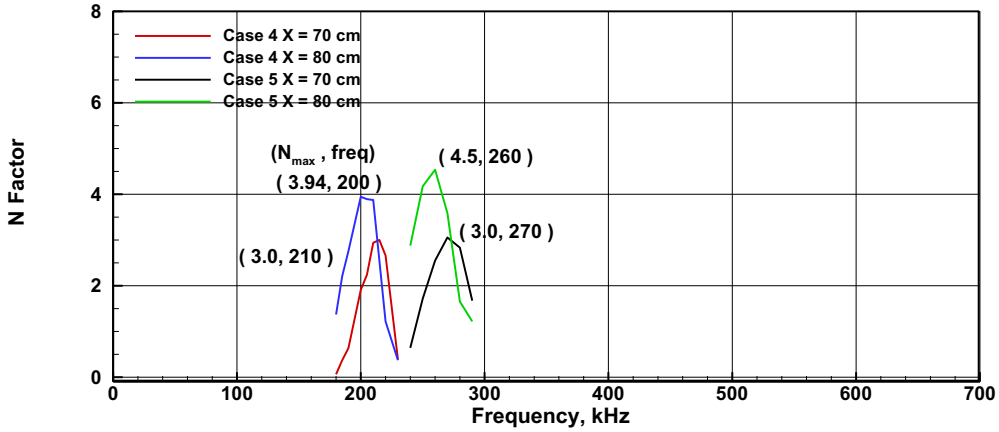

Figure 12. Variation of N-factors with respect to frequency at locations near the measured transition onset locations computed from the PSE analysis and based on $(\rho u)_{max}$ for the Cases 4 and 5.

(c) Interaction of Slow Acoustic Waves with the Cone

Before we performed the transition simulations with a broad spectrum, we investigated the receptivity process by superimposing a single two-dimensional slow acoustic disturbance at the outer computational boundary. Unsteady simulations are performed for several frequencies and the results are presented for the frequencies of 78, 240, and 440 kHz for Cases 1, 2, and 3, respectively. The initial amplitudes of the forcing freestream acoustic disturbances are kept at a constant value of $\tilde{p}_{ac} / p_{\infty} = 2 * 10^{-5}$ in the receptivity investigations.

Figures 13(a-c) show the evolution of the wall pressure fluctuations induced by the slow acoustic wave for the sharp cone, Cases 1, 2, and 3. The figures clearly show the generation and the eventual exponential growth of the instability waves inside the boundary layer. It is seen that the disturbances grow from the leading edge and reach large amplitude levels near the middle of the cone. The results of linear PSE calculations for the same mean boundary layer profile are included in these figures for comparison with the computations. The PSE calculations are initialized at x = 5 cm with the initial conditions obtained from the eigenfunctions obtained from the linear stability calculations. The PSE results are observed to agree very well with the computations starting from $x \sim 30$ cm for Case 1 and starting from $x \sim 10$ cm for the Cases 2 and 3. A receptivity coefficient was defined as the amplitude of the wall-pressure fluctuations at the neutral point nondimensionalized by the freestream acoustic pressure:

$$C_{recpt,p_{wall}} = \frac{(p_{wall})_n}{p_{ac}} \tag{9}$$

The amplitudes of the wall-pressure fluctuations at the neutral points are approximately $7.5*10^{-5}$, $8.0*10^{-5}$, and $9.0*10^{-5}$ for the Cases 1, 2, and 3, respectively. The neutral points are obtained from the PSE results and are located at x = 16, 8, and 5 cm for the three cases, respectively. With those amplitudes, and a freestream acoustic pressure level of $2*10^{-5}$, the receptivity coefficients are approximately 3.75, 4, and 4.5, respectively, for the three cases. The receptivity coefficients increase only slightly with increasing unit Reynolds numbers. The receptivity coefficient for the flow over a sharp 7-deg cone at a freestream Mach number of 6 is about 3.[13] It is seen that the receptivity coefficients in these high Mach number cases are slightly higher but comparable to that at the lower Mach number.

Similarly, Figs. 14 and 15 show the receptivity simulation results for the Cases 4 and 5. Figure 14 shows the density fluctuations inside the boundary layer caused by the interaction of a slow acoustic wave at a frequency of 250 kHz with a blunt cone for Case 5. Figure 14 clearly demonstrates the effect of bluntness in the generation of disturbances near the nose region. As was discussed previously, there exists no entropy layer for the sharp nose case, and the freestream disturbances excited the boundary layer starting at the nose tip. In the large bluntness case, the acoustic disturbances propagate across the leading-edge bow shock and first perturb the entropy layer. It is seen that these disturbances, as they evolve downstream, remain inside the entropy layer and get into the boundary layer farther downstream.

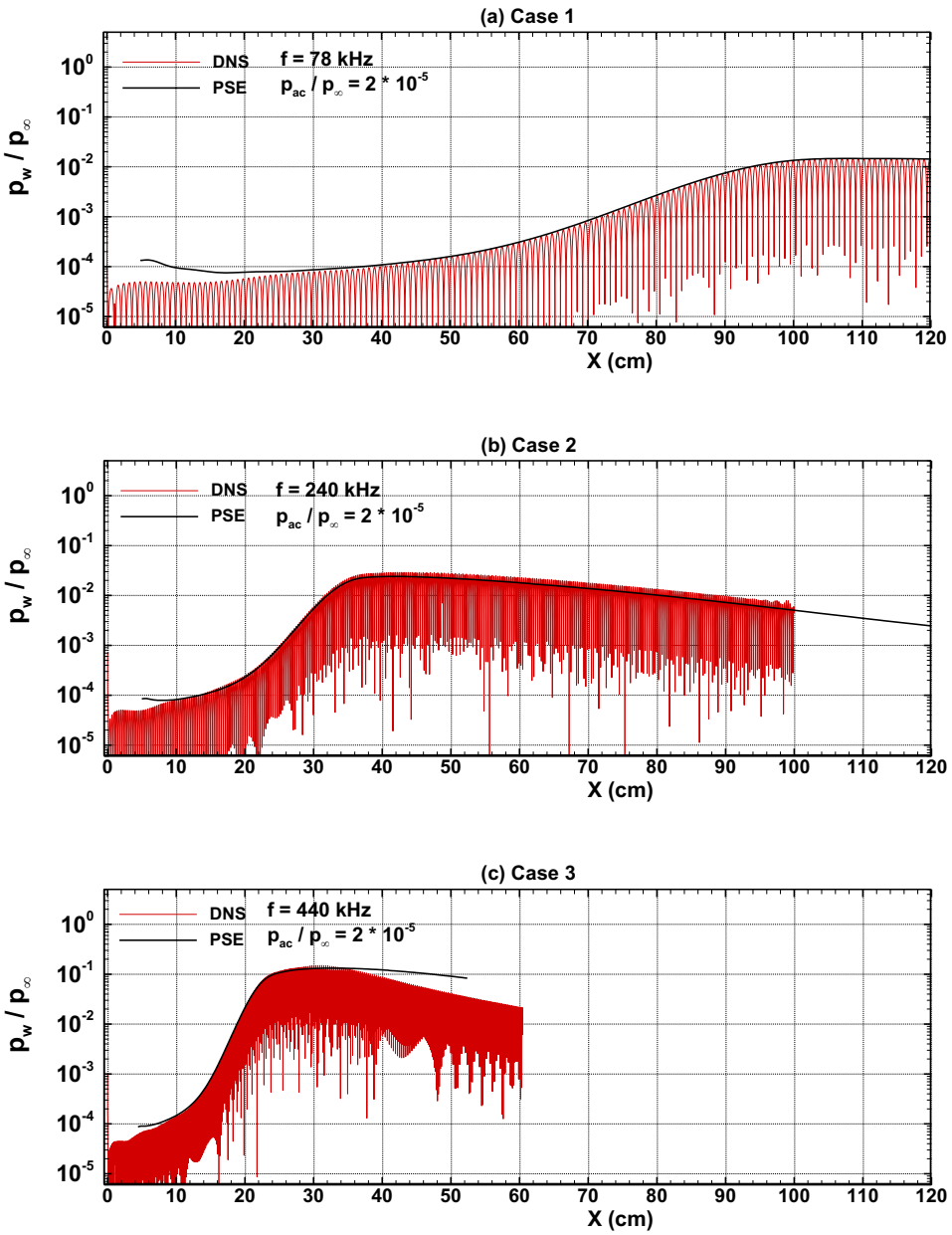

Figure 13. Amplitude of the pressure fluctuations on the wall generated by the slow acoustic wave for the (a) Case 1, (b) Case 2, and (c) Case 3.

Figures 15(a)-(b) show the evolution of the wall pressure fluctuations for these cases. The amplitude of the freestream acoustic pressure is the same, where $p_{ac} / p_\infty = 2 * 10^{-5}$. Since large fluctuations were observed inside the entropy layer, the variations of the maximum mass-flux fluctuations are also plotted in these figures. It is seen that there are large differences in the generation and evolution of disturbances between the sharp nose cases and the blunt nose cases. The figures show that the amplitudes of the wall pressure fluctuations oscillate without growing to

x ~ 60 cm. Beyond that, the disturbances grow exponentially due to the instability of the boundary layer. The maximum mass-flux fluctuation amplitudes initially grow slowly up to x ~ 20 cm and remain almost constant downstream to x ~ 80 cm. Beyond that, the mass-flux fluctuations due to the second-mode instability become larger than the mass-flux fluctuations in the entropy layer. These figures also include the results from the PSE computations. The growth of the disturbances agrees very well with the PSE results in the unstable second mode region. The amplitudes of the wall pressure fluctuations at the neutral points x = 58 cm for Case 4, and x = 60 cm for Case 5 are $2.4*10^{-5}$ and $3.0*10^{-5}$, respectively. The receptivity coefficients are about 1.2 and 1.5 for Cases 4 and 5, respectively. They are about 3 times smaller than that for the sharp cone cases.

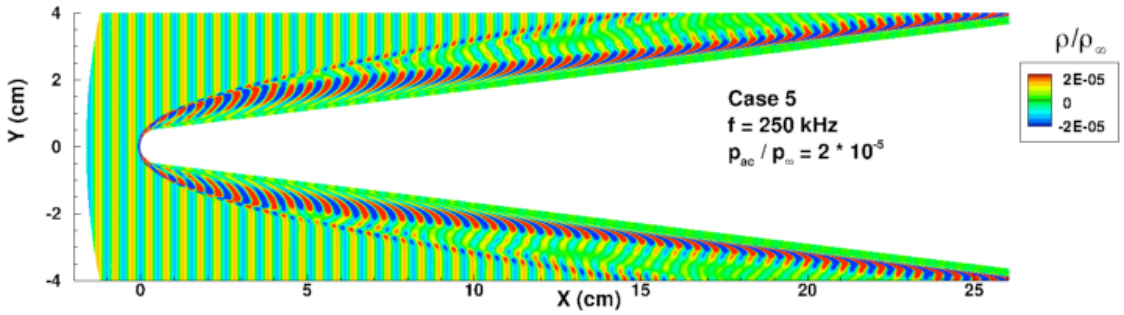

Figure 14. Density fluctuations generated by the interaction of a slow two-dimensional acoustic wave with the blunt cone for Case 5.

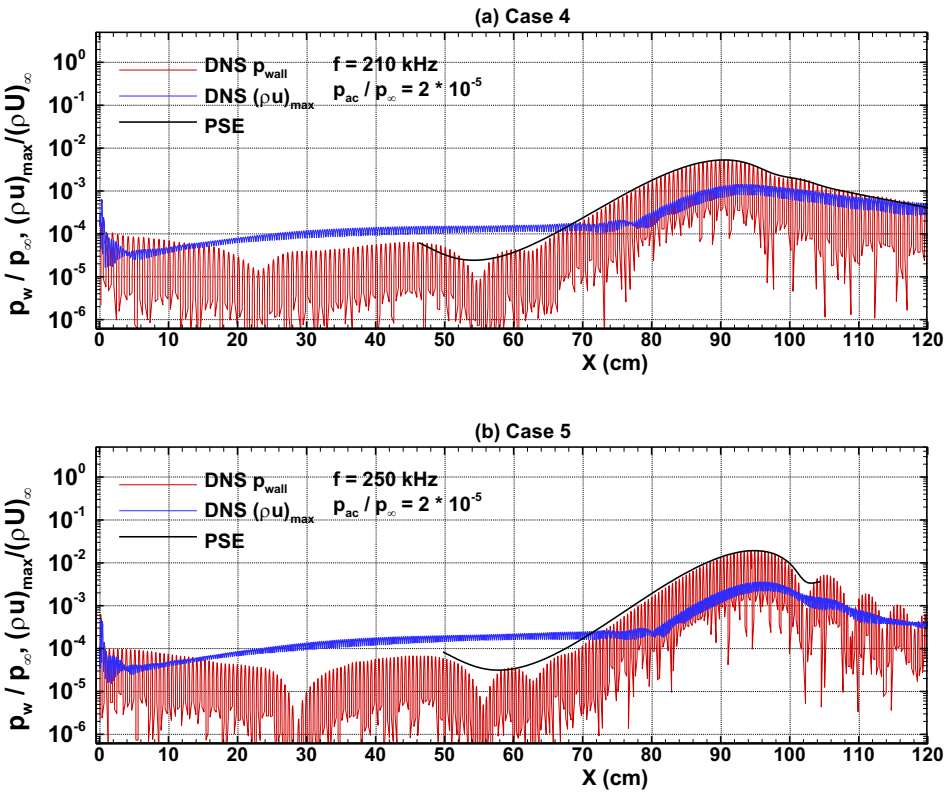

Figure 15. Amplitude of the pressure fluctuations on the wall generated by the slow acoustic wave for the (a) Case 4, and (b) Case 5.

(d) Transition prediction

In this section, the transition prediction results obtained from the simulations by superposing a broad spectrum of slow acoustic disturbances at the outer boundary of the computational domain are presented. As discussed in Sec. 2, the measured broadband spectrum is discretized into a sum of discrete Fourier waves given by Eq. (6). The amplitude of each wave is obtained from the measured spectrum using Eq. (8). The phase angles are selected using random numbers. The number of waves, bin sizes, and the minimum frequencies are selected to span the unstable frequency ranges for each case. The number of waves (*nfmax*), minimum frequencies (f_{min}) in *kHz* and the bin sizes (Δf) in *kHz* for the fives cases are: Case 1 (11, 30, 10), Case 2 (11, 200, 10), Case 3 (21, 390, 10), Case 4 (31, 100, 5), and Case 5 (31, 100, 5).

Figures 16(a) and (b) show the density perturbation contours obtained from the simulations for Case 2. Figure 16(a) depicts the perturbations outside and inside the boundary layer and Fig. 16(b) displays the results inside the boundary layer in a small downstream region. Since the phase angles are constants in time, the freestream forcing is

periodic in time. Figure 16(a) shows that a wave-packet-type forcing occurs in the freestream due to the broadband acoustic disturbances. Figure 16(b) also shows that the disturbances generated are wave packets consisting of all the frequencies convecting downstream and growing in amplitude.

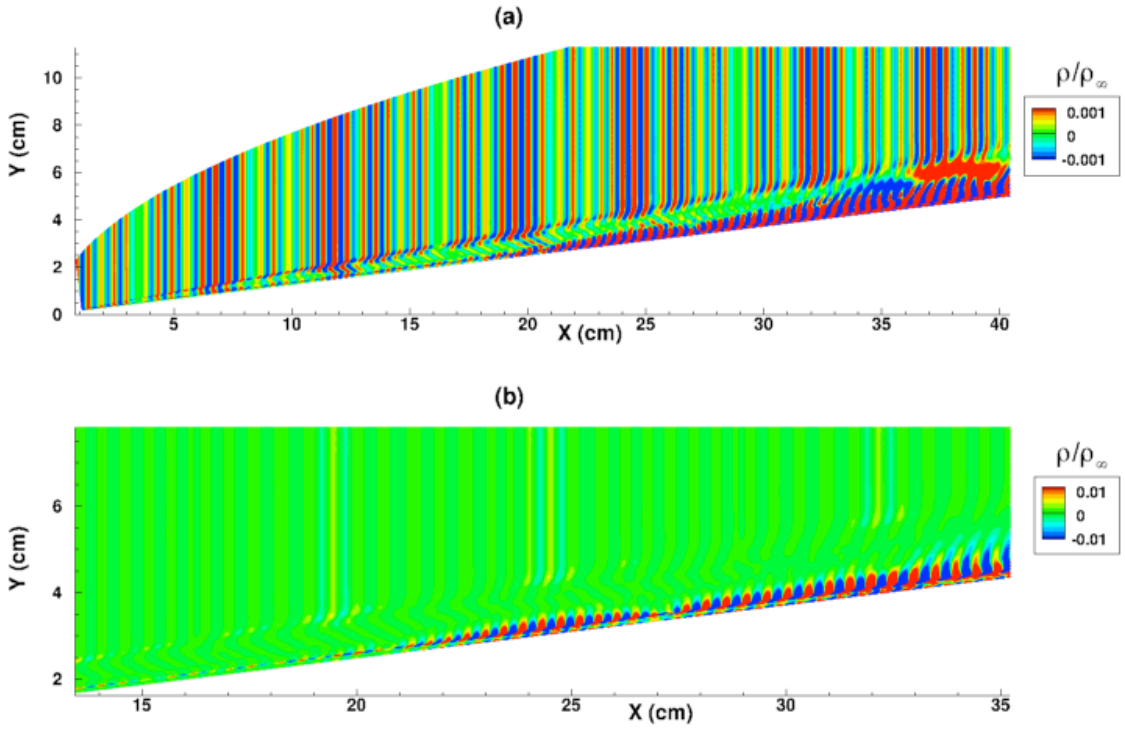

Figure 16. Density fluctuations generated by the interaction of broadband, slow two-dimensional acoustic disturbances with the sharp cone for the Case 2. (a) in a larger domain, and (b) inside the boundary layer.

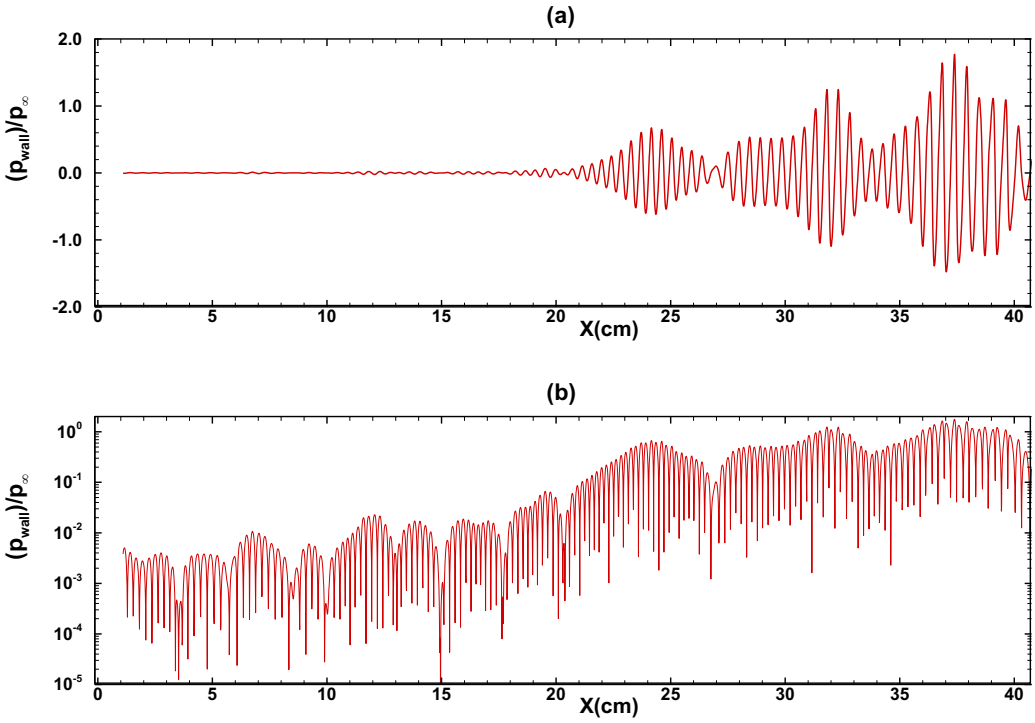

Figure 17. Amplitude of the pressure fluctuations on the wall generated by the slow acoustic waves for the Case 2 (a) in linear-scale, and (b) in log-scale.

Figures 17(a) and (b) show the wall pressure perturbations generated by the interaction of plane two-dimensional acoustic disturbances with the cone for Case 2. Figure 17(a) displays the results in linear-scale and Fig. 17(b) displays the results in a log-scale. These pictures illustrate quantitatively the form and the amplitude variations of the wall pressure fluctuations generated by a broadband acoustic disturbance. As observed in Fig. 16(b), the disturbances at a fixed time consist of a train of wave packets whose amplitudes grow as they travel downstream. Transition onset for this case was measured in the experiment to be around x = 36 cm. It is seen that the amplitude reaches large magnitudes near $x \sim 30$ cm and the amplitude does not grow further downstream.

From the simulation results, the variation of the root mean square (rms) of the pressure fluctuations at the wall, the amplitude spectrum and the power spectral density (PSD) of the wall pressure fluctuations at different axial locations were computed for all five cases. From the computed rms values, the transition onset location was predicted for all of the cases using threshold values of p_{rms} / P_s = 0.10 and 0.20. These values are selected based on the experimentally observed p_{rms} / P_s at the transition onset location, which varied between 0.10 and 0.20.[21] Figures 18-20 show the results for the sharp cone Cases 1, 2, and 3 and Figs. 21 and 24 show the results for the blunt cone Cases 4 and 5.

Figure 18(a) shows the variation of the p_{rms} / P_s along the axial direction for Case 1. First, the simulations were performed with discretized energy for the frequency band between 30 and 130 kHz and random phase angles (indicated by the line marked "random 1"). This frequency range covers the most unstable frequency band. The results are shown in the red solid line in Fig. 18. The experimentally measured rms values are also included as black symbols in Fig. 18(a). The simulation results obtained using this approach follow the trend of measured values, but the computed rms values at fixed axial stations are about two times higher than measured in the experiment. This is the first time comparisons are made between the computed and the measured absolute amplitudes. The predicted transition onset locations based on p_{rms} / P_s = 0.1 and 0.2 are 60 and 76 cm, respectively, for Case 1. The experimentally observed transition onset point is at about 84 cm. The predicted transition onset locations are compared to the measured values in Table 2. The agreement between the computations and the experiment is very encouraging. There may be several reasons for the differences, including the use of plane vs. oblique incident waves, the use of a one-dimensional spectrum vs. a two-dimensional spectrum, etc. Speculation on any specific reason for the difference is not made at this time, but investigating these differences must be pursued both experimentally and computationally to bridge the gap.

Several simulations were also performed to understand the effects of nonlinearity and the bandwidth of the input disturbances. The solid green line displays the evolution of p_{rms} obtained from the linear simulations. These simulations were performed with the same input acoustic waves as the previous simulations, but with the amplitudes of the input waves decreased by a factor of 10. After the simulations, the results were scaled back by 10 times to plot the results. As expected, the linear calculations and the nonlinear calculations are the same up to $x \sim 30$ cm. Beyond that, the rms from the linear calculations grows faster than the nonlinear results. The results reveal that nonlinearity stabilizes the growth of the disturbances. This finding agrees with the observations made by Kuehl et al.[30] We also performed a simulation with a narrower input band of 70 to 100 kHz where the amplitudes of the waves remain the same as the previous simulation. As expected, the rms is initially much smaller than in the full simulation and when the amplitude reaches about 0.10, the results obtained with a narrow band input almost follows the results obtained with the wider band. This shows that the frequency band causing transition is very narrow, in the range of 70-100 kHz. A simulation was also performed with only one frequency input. This was the approach used in the past. The results obtained for a frequency of 80 kHz are shown in Fig. 18(a). As expected, the p_{rms} / P_s reaches a value 0.10 farther downstream, at about 78 cm, compared to the full simulation.

Figure 18(b) shows the computed amplitude (rms) spectra at an axial location of x = 80 cm. The results obtained with the linear simulations are depicted. The amplitude with the full simulation (random 1) is smaller than that obtained by the linear calculations. It agrees with the previous observation that nonlinearity stabilizes the growth of the disturbances. The amplitude peaks at about 90 kHz and the maximum amplitude is about 0.50. If the frequency band with amplitudes at $1/5^{th}$ of the maximum amplitude is selected as the dominant frequencies, the bandwidth of the most amplified frequencies ranges from 70 to 100 kHz. Figure 18(c) shows the computed and measured power spectral density (PSD) at the same axial location, x = 80 cm. The computed shape of the PSD and the peak frequency agree very well with the measurements. The maximum computed PSD amplitude is about an order higher than the measured value. We observed a similar behavior in the rms comparison.

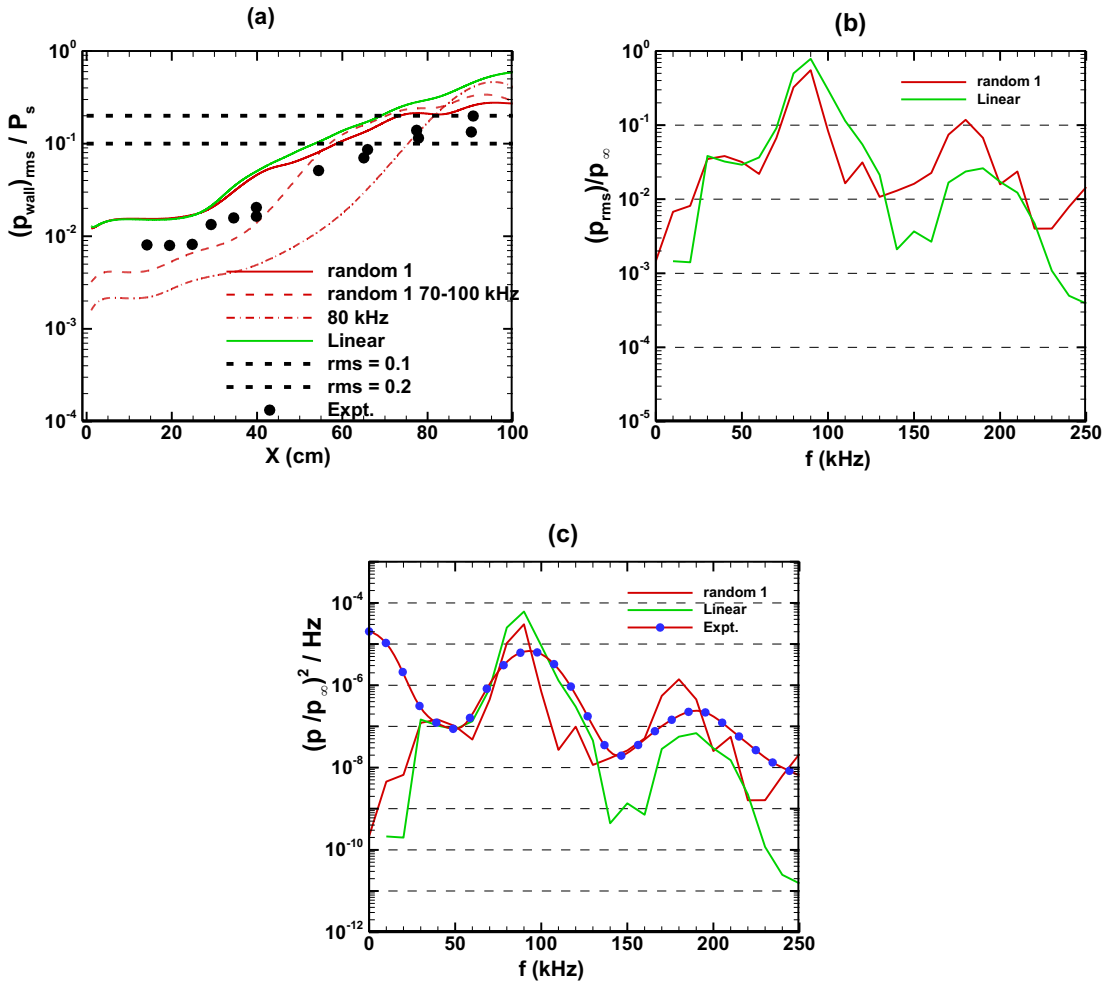

Figure 18. (a) Variations of the rms of the wall pressure fluctuations along the cone, (b) spectral amplitude of the pressure fluctuations at x = 80 cm, and (c) power spectral density at x = 80 cm for Case 1.

Similarly, Figures 19 and 20 show the results for the Cases 2 and 3. Figure 19(a), (b) and (c) display the results obtained from several simulations for Case 2. The bandwidth of the input frequencies in this case is from 200 to 300 *kHz* and the bin size is 10 *kHz*. The simulations were performed with four random number sets for the phase angles. The results are denoted as random 0, 1, 2, and 3 in the figures. The results shown by the line marked "random 0" are obtained with zero phase angles. A linear simulation was also performed, as described above, and one simulation was performed with a single frequency input of f = 240 *kHz*. Figure 19(a) displays the variation of the rms of the wall pressure fluctuations, p_{rms}, obtained from several simulations. The experimentally measured rms values are also included as black symbols in Fig. 19(a). The simulation results obtained using this approach follow the measured

values. The computed rms values at fixed axial stations also agree well with the measurements in this case. The disturbances evolve linearly up to $x \sim 26$ cm. Beyond that, the growth of the disturbances deviates from the linear theory and the growth is stabilized by the nonlinearity. Another observation is that the evolution of the disturbances with no phase difference behaves differently compared to the disturbances obtained with the random phase angles. The growth is strongly stabilized by the nonlinearity in the no-phase-angle case compared to the other cases. The results with the single frequency input grow exponentially according to linear theory and decay beyond $x \sim 36$ cm. The predicted transition onset locations based on $p_{rms} = 0.1$ and 0.2 are 28 and 36 cm, respectively, for Case 2. The experimentally observed transition onset location is at about 36 cm. Figure 19(b) shows the computed amplitude (rms) spectra at an axial location of $x = 30$ cm. The results obtained with the linear simulation are included here. The amplitudes with the full simulations are slightly smaller than that obtained with the linear calculation. The amplitude peaks at about 260 *kHz* and the maximum amplitude is about 0.25. The bandwidth of the most amplified frequencies are in the range of 225 to 300 *kHz*. Figure 19(c) shows the computed and measured power spectral density (PSD) distributions at the same axial location $x = 30$ cm. The computed shape of the PSD and the peak frequency agree very well with the measurements. Similar to Case 1, the maximum computed PSD amplitude is about an order of magnitude higher than the measured value.

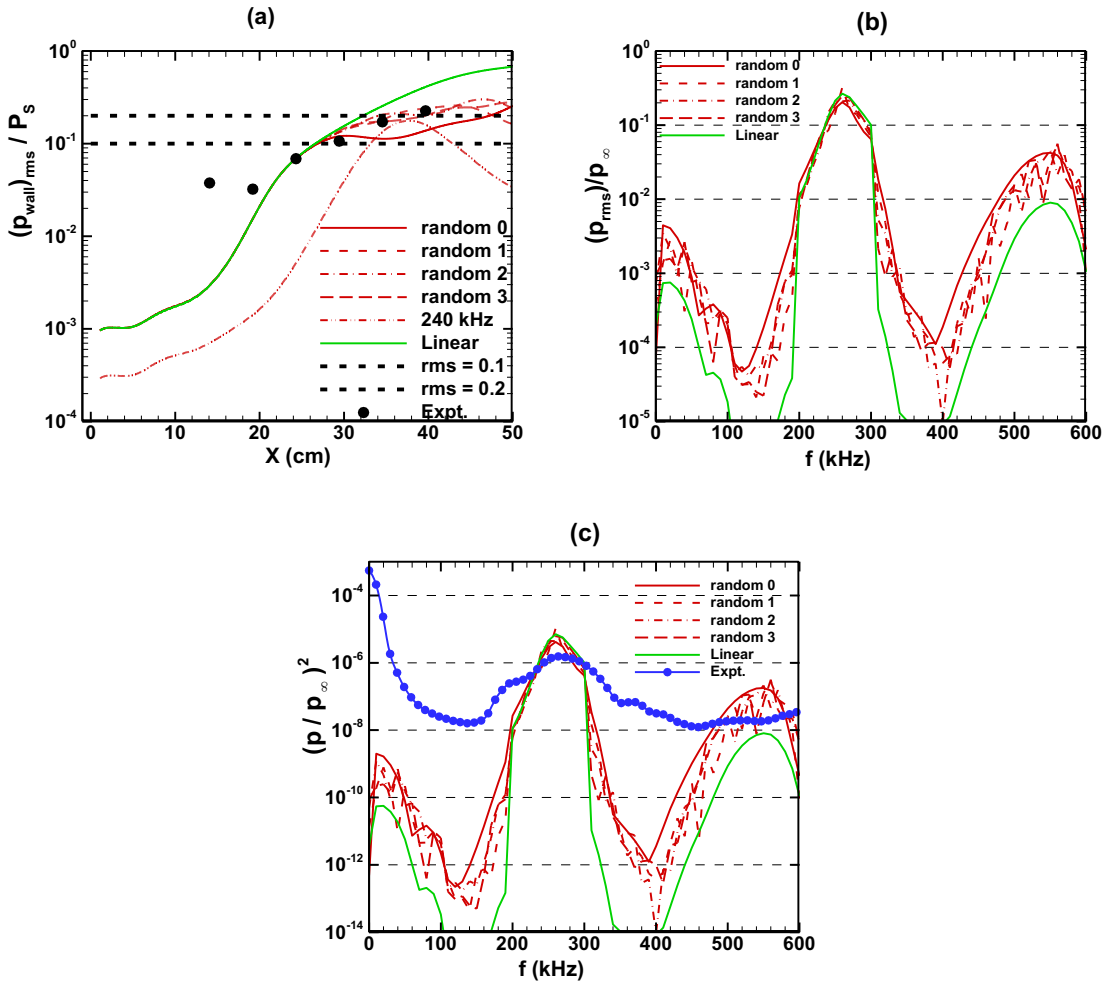

Figure 19. (a) Variations of the rms of the wall pressure fluctuations, (b) spectral amplitude of the pressure fluctuations at x = 30 cm, and (c) power spectral density at x = 30 cm for Case 2.

Figures 20(a), (b) and (c) show the variation of the rms, the spectral amplitude, and the PSD of the wall pressure fluctuations at x = 20 cm, respectively, for Case 3. The bandwidth of the input frequencies in this case ranges from 390 to 590 kHz and the bin size is 10 kHz. As in the previous cases, simulations are performed with three random phase angle sets, one linear case, and one with a single frequency input of 490 kHz. The experimentally measured rms values are also included as black symbols in Fig. 20(a). The simulation results obtained using this approach differ from the measured values below x < 25 cm. Beyond that, the computed rms values follow the trend of the measured values. The observations are similar to the previous cases. The disturbances evolve linearly up to x ~ 16 cm and, beyond that, nonlinear effects stabilize the growth. The predicted transition onset locations based on p_{rms} = 0.1 and 0.2 are 17 and 21 cm, respectively. The experimentally observed transition onset location is at about 25 cm.

Figure 20(b) shows the computed amplitude (rms) spectra at an axial location of x = 20 cm. The results obtained with the linear simulations are included here. Similar to the previous cases, the amplitude of the rms pressure fluctuations with the full simulation are slightly smaller than that obtained with the linear calculations. The amplitude peaks at about 490 *kHz* and the maximum amplitude is about 0.21. The bandwidth of the most amplified frequencies are from 440 to 590 kHz. Figure 20(c) similarly shows the computed and measured power spectral density (PSD) distributions at the same axial location x = 20 cm. The computed shape of the PSD and the peak frequency agree very well with the measurements. In this case compared to the previous two cases, the computed PSD amplitudes also agree very well with the measurements. Overall, the predicted transition locations and the PSD shapes and the unstable frequency range agree well with the measurements for the Cases 1, 2 and 3.

The predicted maximum N-factors at the transition onset points obtained from the linear PSE calculations for the sharp nose Cases 1, 2, and 3 are N_{case1} = 4.0, N_{case2} = 5.1, and N_{case3} = 6.7, respectively. Hence, the N-factors at the transition onset location for the same geometry and in the same tunnel gradually increase with the unit Reynolds numbers. The initial amplitudes of the pressure fluctuations, p_{rms}, at $x \sim 1.0$ cm obtained from the Figs. 18, 19, and 20 are about $1.0*10^{-2}$, $1.0*10^{-3}$, and $4.0*10^{-4}$, respectively. The initial rms contains contributions from all the frequencies, not only the contribution from the frequency band that causes the transition. The initial amplitudes are about 10 and 25 times smaller in Cases 2 and 3 compared to Case 1. Hence, the reason for the increasing N-factors with unit Reynolds numbers is that the frequency band that causes the transition is centered at higher frequencies and the freestream noise level decreases with increasing frequency.

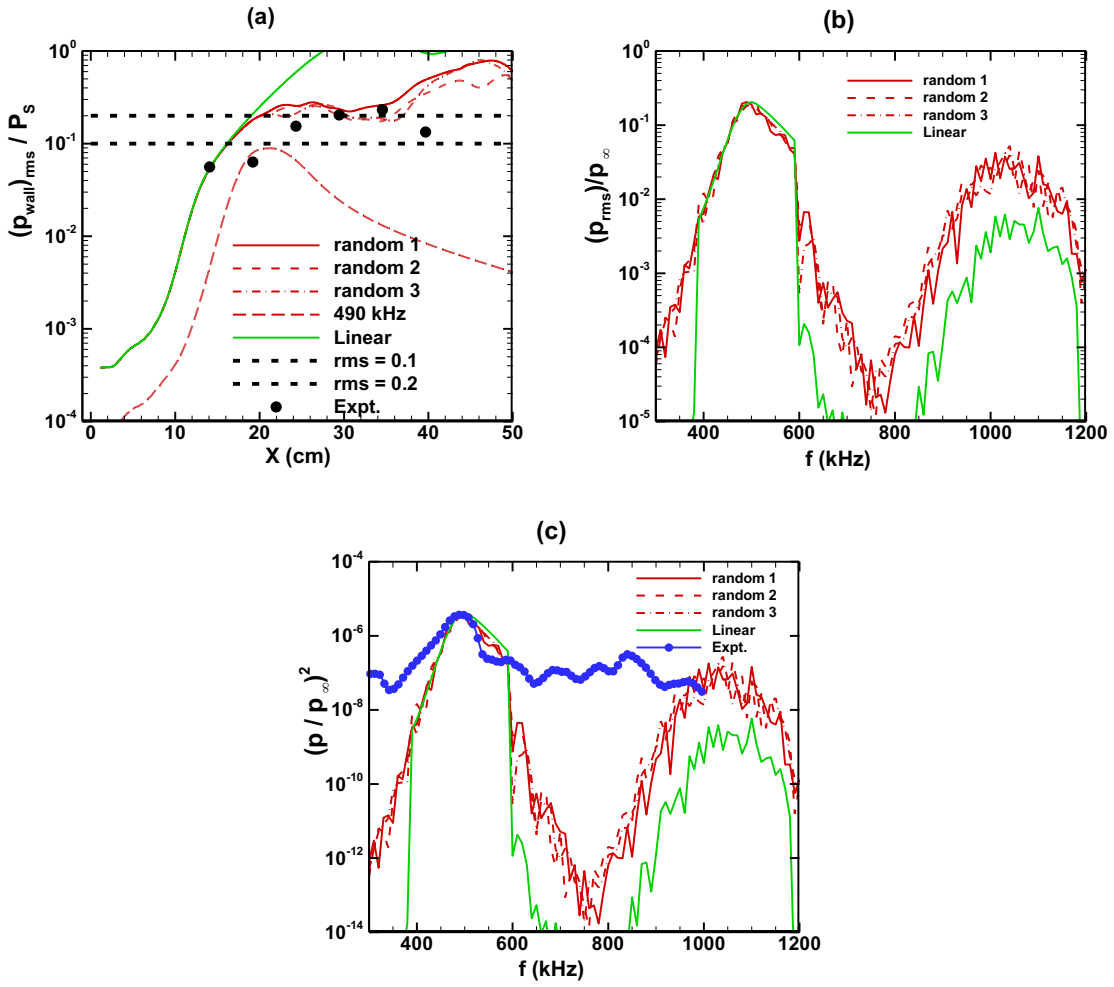

Figure 20. (a) Variations of the rms of the wall pressure fluctuations along the cone, (b) spectral amplitude of the pressure fluctuations at x = 20 cm, and (c) power spectral density at x = 20 cm for Case 3.

Figures 21-24 show the simulation results for the blunt nose Cases 4 and 5. Similar to Figs. 16(a) and (b), Figs. 21(a) and (b) show the density perturbations contours obtained from the simulations for Case 5. Similar results were obtained for Case 4. Figure 21(a) depicts the perturbations outside and inside the boundary layer and Fig. 21(b) displays the results inside the boundary layer in a downstream region. Figure 21(a) shows the wave packet type forcing that occurs in the freestream. Figure 21(b) also shows that the disturbances generated are wave packets consisting of all the input frequencies. As we observed in the receptivity simulations results for the flow over the blunt cone in Fig. 14, Fig. 21(a) shows that the disturbances are first generated inside the entropy layer near the nose region. Figures 22(a) and (b) show the wall pressure perturbations generated by the interaction of plane two-

dimensional acoustic disturbances with the cone for Case 5. Figure 22(a) displays the results in linear-scale and Fig. 22(b) displays the results in log-scale. These pictures quantitatively illustrate the form and the amplitude variations of the wall pressure fluctuations generated by a broadband acoustic disturbance. The disturbances at a fixed time consist of a train of wave packets whose amplitudes slowly decrease up to $x \sim 75$ cm. Beyond that, the disturbances grow due to the second-mode instability. The transition onset for this case occurred in the experiment around $x = 68$ cm. It is seen that the disturbances did not start to grow until $x \sim 80$ cm in this case.

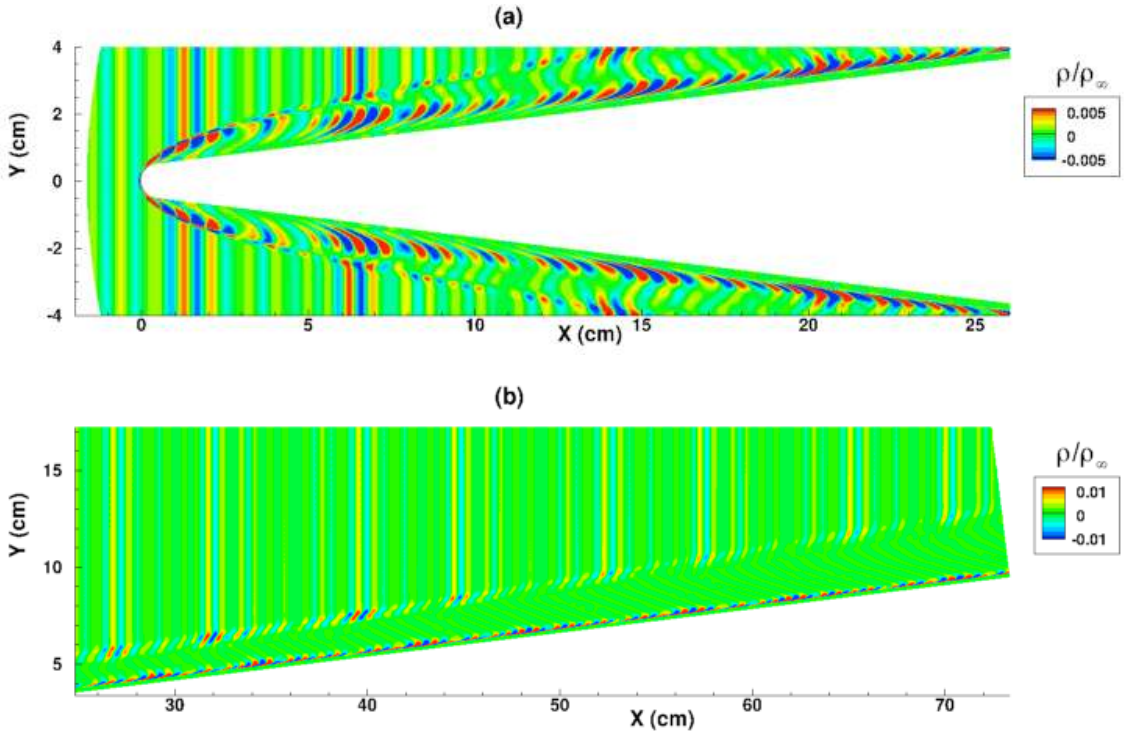

Figure 21. Density fluctuations generated by the interaction of broadband slow two-dimensional acoustic disturbances with the sharp cone for Case 5. (a) in a larger domain, and (b) inside the boundary layer.

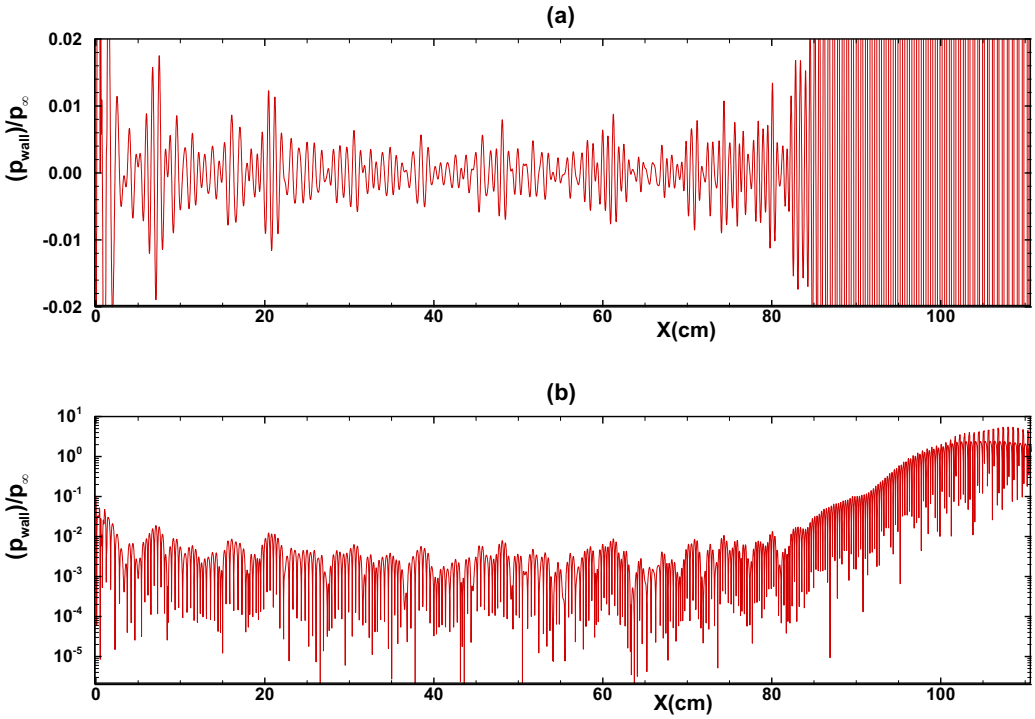

Figure 22. Amplitude of the pressure fluctuations on the wall generated by the slow acoustic waves for Case 5 (a) in linear scale, and (b) in log-scale.

Figures 23(a), (b) and (c) show the variation of the rms of the wall pressure fluctuations along the cone, the spectral amplitude and the PSD of the wall pressure fluctuations at x = 90 cm, respectively, for Case 4. The bandwidth of the input frequencies in this case is from 130 to 280 *kHz* and the bin size is 5 *kHz*. As in the previous cases, simulations are performed with two random phase angle sets, and one linear case. The experimentally measured rms values are also included as black symbols in Fig. 23(a). The measured rms values are about an order of magnitude larger than the computed values in the region x < 60 cm. Beyond that, the growth of the measured and the computed rms follow the same slope approximately, but the measured amplitudes are higher than the computed values. Also, the measured rms amplitudes peak much earlier compared to the computed results. The observations are similar to the previous cases. However, in this case, the disturbances evolve linearly up to x ~ 100 cm, which is well beyond the transition onset point. The experimentally observed transition onset location is at about 68 cm. The predicted transition onset locations based on p_{rms} = 0.1 and 0.2 are 92 and 96 cm, respectively. Hence the transition onset location is over-predicted by this method by 24 to 28 cm. It is possible that the simulations must consider acoustic waves impinging the cone at an incident angle rather than at 0° to obtain a better prediction. Figure 23(b)

shows the computed amplitude (rms) spectra at an axial location of x = 90 cm for both the full simulation and the linear simulation. The amplitude with the full simulation is almost the same as that obtained with the linear simulations. The amplitude peaks at about 200 *kHz* and the maximum amplitude is about 0.05. The bandwidth of the most amplified frequencies are from 180 to 210 *kHz*. Hence the bandwidth of the dominant frequency band is very narrow, on the order of 30 *kHz*. Figure 23(c) similarly shows the computed and measured power spectral density (PSD) distributions at the same axial location x = 90 cm. The computed shape of the PSD is narrower than the measured spectrum. However, the computed peak frequency agrees with the measurement. At this point, we do not know why the measured spectrum is broader than that predicted by the linear theory.

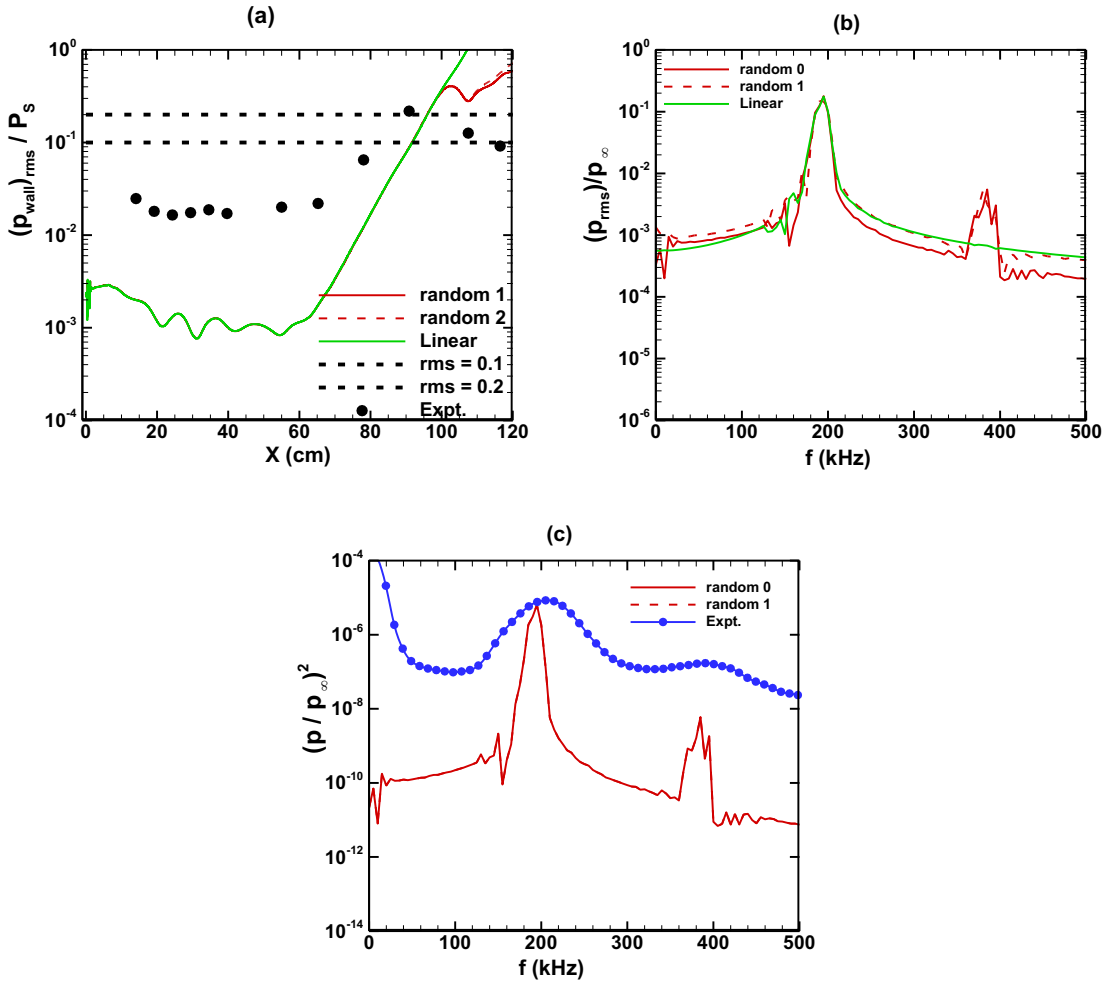

Figure 23. (a) Variations of the rms of the wall pressure fluctuations along the cone, (b) spectral amplitude of the pressure fluctuations, and (c) power spectral density at x = 90 cm for Case 4.

Figures 24(a), (b) and (c) show the variation of the rms of the wall pressure fluctuations along the cone, the spectral amplitude and the PSD of the wall pressure fluctuations at x = 90 cm, respectively, for Case 5. The bandwidth of the input frequencies in this case is from 130 to 280 *kHz* and the bin size is 5 *kHz*. The observations are similar to Case 4. The measured rms values differ from the predicted values. The measured rms values are larger than the predicted values up to $x \sim 90$ cm. The measured rms values peak around $x \sim 90$ cm and decrease downstream. The measured maximum rms value is about 0.10 and is much lower than the predicted values. As discussed earlier, the measured transition onset point is also at $x \sim 68$ cm, as in the low Reynolds number case, Case 4. The predicted transition onset locations based on p_{rms} = 0.1 and 0.2 are 90 and 93 cm, respectively. Again, the transition onset point is overpredicted by 22 to 25 cm using this method. However, the predicted transition onset point for Case 5 is at the same location as for Case 4, which is similar to what was observed in the experiment. Figure 24(b) shows the computed amplitude (rms) spectra at an axial location of x = 90 cm. The amplitude peaks at about 255 kHz and the maximum amplitude is about 0.025. The bandwidth of the most-amplified frequencies ranges from 230 to 270 kHz. Hence, the bandwidth of the dominant frequency band is very narrow as in the previous case, on the order of 40 kHz. Figure 24(c) similarly shows the computed and measured power spectral density (PSD) distributions at the same axial location x = 90 cm. Similar to the previous Case 4, the computed spectrum is narrower than the measurement. The computed most amplified frequency range agrees with the measurement. The computed peak PSD amplitude is about an order higher than the measurement. Overall, the agreements between the prediction and measurements for the blunt nose cases are not as good as for the sharp cone cases. We have to explore these cases further to explain these observed differences.

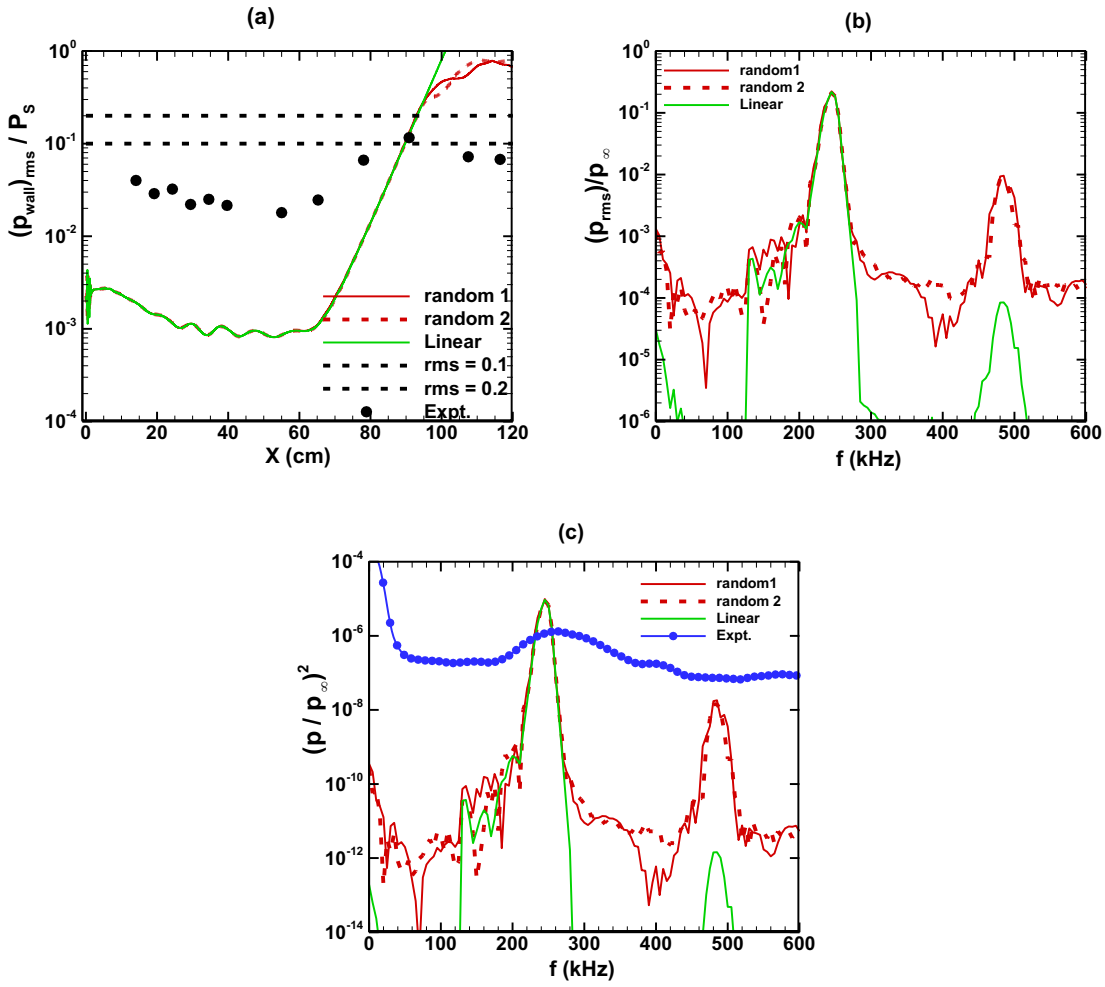

Figure 24. (a) Variations of the rms of the wall pressure fluctuations, (b) spectral amplitude of the pressure fluctuations at x = 90 cm, and (c) power spectral density at x = 90 cm for Case 5.

V. Discussion and Conclusion

The transition onset locations on a 7-degree half-angle cone at different unit Reynolds numbers in hypersonic flow at a freestream Mach number of 10 were predicted using freestream spectra, receptivity, linear and weakly nonlinear growth, and a threshold amplitude for transition onset. The geometry and the freestream conditions were the same as in the experiment.[21] We performed the simulations for two nose radii, one sharp and the other a medium bluntness. The unit Reynolds number was varied from small to large values in both cases. The only input into the simulations was the measured freestream spectrum of the pressure perturbations. We assumed the spectrum contains only one-dimensional plane acoustic disturbances. As it was done in Ref. 21, we assumed an $f^{-3.5}$ variation for the

measured freestream spectrum. We represented the measured spectrum as a sum of discrete two-dimensional plane slow acoustic waves. The amplitude of each wave was obtained by equating the energy in each wave with the energy in the measured spectrum within a small bin. The acoustic waves were superposed at the outer boundary of the computational domain and time accurate two-dimensional simulations were performed to investigate the generation and evolution of disturbances inside the boundary layer. Both the steady and unsteady solutions were obtained by solving the two-dimensional Navier-Stokes equations in axisymmetric coordinates using a 5^{th}-order accurate, weighted essentially nonoscillatory (WENO) scheme for space discretization and using a third-order total-variation-diminishing (TVD) Runge-Kutta scheme for time integration.

The computed mean profiles were analyzed by using local stability and nonlocal parabolized stability equations (PSE) methods. The results for the sharp nose cases showed that the boundary layer profiles approach the similarity profiles within a short distance from the tip of the cone. The maximum N-factors at the measured transition onset locations increased gradually with the unit Reynolds number. It was also observed that the most amplified frequencies and the band of unstable frequencies also increased with the unit Reynolds number. The results for the blunt nose cases showed that the flow fields near the nose region were dominated by the entropy layers that were generated by the bow shocks formed in front of the blunt nose. No discernable boundary layers were observed in the nose region for the flow over blunt cones. The entropy layer persisted for about 100 nose radii downstream and eventually merged with the boundary layer developing along the wall. The boundary layer remained stable until the merging of the entropy and the boundary layers. The maximum N-factors at the measured transition onset locations were small compared to the sharp nose cases at the comparable unit Reynolds numbers. It was also observed that the measured transition onset locations and the computed N-factors were the same for the small and large Reynolds numbers. The unstable frequency bands were also very narrow compared to the sharp nose cases at comparable unit Reynolds numbers.

The receptivity simulations with a single acoustic wave revealed that the receptivity coefficients increase mildly with the unit Reynolds number for the flows over sharp cones. The receptivity coefficients based on the wall pressure fluctuations near the nose region are about 4 times the amplitude of the freestream acoustic wave. The simulations for the blunt nose cases showed that the wall pressure fluctuations slowly decay for long distances before they grow again due to the second mode instability. The receptivity coefficients are smaller, on the order of 1, compared to flow over sharp cone cases. It was also observed that large density fluctuations are generated inside the

entropy layer. These fluctuations initially grew slightly and remained almost constant for long distances until they grew again due to the second mode instability.

The transition onset locations were predicted by incorporating the freestream spectrum, receptivity, linear and nonlinear evolution, and a threshold for the amplitude of the wall pressure fluctuations. The predicted transition onset locations are close, within 10%, to the measured locations for the sharp nose cases. The computed rms values of the wall pressure fluctuations are about two times smaller than the measured values. However, the variations follow the same trend as predicted by the simulations. The predicted PSD also agree in shape and frequency range. However, the predicted amplitudes are an order of magnitude higher than the measured values. Overall, the agreements between the computations and the experiment are very encouraging. There may be many known and unknown reasons for the differences, including the use of plane vs. oblique incident waves, the use of a one-dimensional spectrum vs. a two-dimensional spectrum, etc. Speculation on any specific reason for the difference is not made at this time, but investigating these differences must be pursued both experimentally and computationally to bridge the gap.

The comparisons for the blunt nose cases are not as good as that for the sharp cone cases. The transition onset locations are overpredicted by about 30% compared to the measurements. The disturbances started to grow earlier in the experiment than was predicted. The measured PSD are broader than the computed spectrum. But the predicted most amplified frequencies and the peak amplitudes agree well with the experiment.

In this paper, we attempted to predict transition onsets for flow over cones using measured freestream spectrum and two-dimensional numerical simulations. The approach provided encouraging results for widely different flow conditions. The question is how can we improve the prediction further? As we mentioned earlier, we considered only plane two-dimensional acoustic waves in the simulations. In wind tunnels, the noise is radiated from the nozzle walls at oblique angles. We have to consider acoustic disturbances impinging the cone at oblique angles in the simulations. The predictions for the flow over a medium blunt cone were not very satisfactory. The prediction of transition in flows over blunt geometries continues to be a challenging problem. In the present simulations, we observed large oscillations inside the entropy layer. One possibility is to consider three-dimensional freestream disturbances in the simulations and see whether they introduce any large oscillations and cause early transition. In addition, off-body instability measurements inside the boundary and entropy layers are needed to identify mechanisms that are responsible for transition in flows over blunt geometries.

References

[1]Morkovin, M. V., Reshotko, E., and Herbert, T., "Transition in Open Flow Systems – a reassessment," *Bull. APS*, Vol. 39, No. 9, pp. 1882, 1994.

[2]Mack, L., "Boundary Layer Stability Theory," *JPL Report No. 900-277 Rev. A*, Pasadena, Calif, Nov. 1969.

[3]Kendall,J. M., "Wind Tunnel Experiments Relating to Supersonic and Hypersonic Boundary-Layer Transition ," *AIAA J.,* Vol. 13, No. 3, 1975, pp. 290-299.

[4]Stetson, K. F., Thompson, E. R., Donaldson, J. C., and Siler, L. G., "Laminar Boundary Layer Stability Experiments on a Cone at Mach 8, Part 1: Sharp Cone," AIAA 22nd Aerospace Sciences Meeting, Reno, Nevada, January 9-12, *AIAA Paper 83-1761*, 1983.

[5]Stetson, K. F., and Kimmel, R. L., "On Hypersonic Boundary-Layer Stability," *AIAA Paper 92-0737*, January 1992.

[6]Blanchard, A.E., "An Investigation of Wall-Cooling Effects on Hypersonic Boundary-Layer Stability in a Quiet Wind Tunnel", Ph.D. Dissertation, Old Dominion University, Dept. of Mechanical Engineering, Norfolk, VA, December, 1995.

[7]Lachowicz, J, T., Chokani, N., and Wilkinson, S.P., "Boundary-Layer Stability Measurements in a Hypersonic Quiet Tunnel", *AIAA Journal*, Vol. 34, No. 12, December 1996.

[8]Wilkinson, S. P., "A Review of Hypersonic Boundary Layer Stability Experiments in a Quiet Mach 6 Wind Tunnel", *AIAA Paper 97-1819*, June 1997.

[9]Maslov, A. A., Shiplyuk, A. N., Sidorenko, A. A and Arnal, D., "Leading Edge Receptivity of a Hypersonic Boundary layer on a Flat Plate," *J. Fluid Mech.,* Vol. 426, 2001, pp. 73-94.

[10]Wheaton, B., Juliano, T.J., Berridge, D.C., Chou, A., Gilbert, P.L., Casper, K.M., Steen, L.E., Schneider, S., and Johnson, H.B., "Instability and Transition Measurements in the Mach 6 Quiet Tunnel," *AIAA Paper 2009-3559*, June 2009.

[11]Berridge, D.C., Chou, A., Ward, A. C., Steen, L.E., Gilbert, P. L., Juliano, T. J., Schneider, S., and Gronvall, J. E., "Hypersonic Boundary-Layer Transition Experiments in a Mach-6 Quiet Tunnel," *AIAA Paper 2010-1061*, January 2010.

[12]Casper, K.M., Beresh, S.J., Henfling, J.F., Spillers, R.W., Pruett, B., and Schneider, S.P., "Hypersonic Wind-Tunnel Measurements of Boundary-Layer Pressure Fluctuations," *AIAA Paper 2009-4054*, Jun 2009.

[13]Balakumar, P., and Kegerise, M. A., "Receptivity of Hypersonic Boundary Layers over Straight and Flared Cones," *AIAA Paper 2010-1545*, January 2010.

[14]Kocian, T., Perez, E., Oliviero, N., Kuehl, J. J., and Reed, H. L., "Hypersonic Stability Analysis of a Flared Cone,", AIAA 2013-0667.

[15]Malik, M.R., "eMalik3d: An e^N Code for Three-Dimensional Flow over Finite-Swept Wings", High Technology Report No. HTC-9502, 1995.

[16]Chang, C. L., "The Langley stability and transition analysis code (LASTRAC) version 1.2 user manual," NASA/TM-2004-2133233, June 2004.

[17]Johnson, H. B., and Candler, G. V., "Hypersonic Boundary Layer Stability Analysis Using PSE-Chem," AIAA Paper 2005-5023.

[18]Stetson, K. F., Thompson, E. R., Donaldson, J. C., and Siler, L. G., 1984, "Laminar Boundary Layer Stability Experiments on a Cone at Mach 8, Part 2: Blunt Cone," *AIAA Paper*, 0006

[19]Kara, K., Balakumar, P. and Kandil, O. A., "Effects of Nose Bluntness on Hypersonic Boundary Layer Receptivity and Stability over Cones," *AIAA Journal*, Vol. 49, No. 12, December 2011, pp. 2593-2606.

[20]Balakumar, P., "Receptivity of Hypersonic Boundary Layers to Acoustic and Vortical Disturbances (Invited)," AIAA Paper 2015-2473.

[21]Marineau, E. C., Moraru, C. G., Lewis, D. R., Norris, J. D., Lafferty, J. F., and Johnson, H. B., "Investigation of Mach 10 Boundary-Layer Stability of Sharp Cones at Angle-of-Attack, Part 1: Experiments", AIAA Paper, 2015-1737.

[22]Mack, L. M., "Transition and Laminar Instability," NASA-CP-153203, Jet Propulsion Lab, Pasadena, California, 1977.

[23]Fedorov, A. V., "Applications of the Mack Amplitude Method to Transition Predictions in High-Speed Flows," NATO RTO-MP-AVT-200, 2012.

[24]Marineau, E. C., Moraru, C. G., Lewis, D. R., Norris, J. D., and Lafferty, J. F., "Mach 10 Boundary-Layer Transition Experiments on Sharp and Blunted Cones", AIAA Paper, 2014-3108.

[25]Johnson, H. B., Marieneau, E. C., Moraru, C. G., Lewis, D. R., Norris, J. D., and Lafferty, J. F., "Investigation of Mach 10 Boundary Layer Stability of Sharp Cones at Angle-of-Attack, Part 2: Computations," AIAA Paper , 2015-1738.

[26]Shu, C. W., 1997, Essentially Non-Oscillatory And Weighted Essentially Non-Oscillatory Schemes For Hyperbolic Conservation Laws, NASA/CR-97-206253 and ICASE Report No. 97-6.

[27]Atkins, H. L., 1991, High-Order ENO Methods for the Unsteady Compressible Navier-Stokes Equations, AIAA Paper, 1557.

[28]Balakumar, P., 2002, Stability of Hypersonic Boundary Layers Over a Compression Corner, AIAA Paper, 2848.

[29]Kara, K., Balakumar, P., and Kandil, O. A., "Effects of Nose Bluntness on Stability of Hypersonic Boundary Layers over Blunt Cone," 37th AIAA Fluid Dynamics Conference and Exhibit, Miami, FL, AIAA 2007-4492.

[30]Kuehl, J. J., Reed, H. L., Kocian, T. S., and Oliviero, N. B., "Bandwidth Effects on Mack-Mode Instability", AIAA Paper, 2014-2777.